Supplemental information

Suppressing phase segregation and nonradiative losses by a multifunctional cross-linker for high-performance all-perovskite tandem solar cells

Xin Zheng[a] ‡ , Shaomin Yang[a] ‡ , Jingwei Zhu[c] ‡ , Ranran Liu[a], Lin Li[a,f], Miaomiao Zeng[a], Chunxiang Lan[a], Shangzhi Li[a], Jinghao Li[b], Yingying Shi[a], Cong Chen[c], Rui Guo[a], Ziwei Zheng[d], Jing Guo[g], Xiaoyu Wu[d], Tian Luan[d], Zaiwei Wang[e], Dewei Zhao[c]*, Yaoguang Rong[b]* and Xiong Li[a,d]*

[a] *Michael Grätzel Center for Mesoscopic Solar Cells, Wuhan National Laboratory for Optoelectronics, Huazhong University of Science and Technology, Wuhan 430074, Hubei, China. E-mail: xiongli@hust.edu.cn*
[b] *School of Chemistry, Chemical Engineering and Life Sciences, State Key Laboratory of Advanced Technology for Materials Synthesis and Processing, Wuhan University of Technology, Wuhan 430070, Hubei, China. E-mail: ygrong2022@outlook.com*
[c] *College of Materials Science and Engineering & Engineering Research Center of Alternative Energy Materials & Devices, Ministry of Education, Sichuan University, Chengdu 610065, Sichuan, China. E-mail: dewei.zhao@scu.edu.cn*
[d] *School of Physics and Optoelectronic Engineering, Hainan University, Haikou 570228, Hainan, China.*
[e] *Institute of Technology for Carbon Neutrality, Shenzhen Institute of Advanced Technology, Chinese Academy of Sciences, Shenzhen 518055, Guangdong, China.*
[f] *Institute of New Materials and Advanced Manufacturing, Beijing Academy of Science and Technology, Beijing 100089, China.*
[g] *Center for Advanced Studies in Precision Instruments, Hainan University, Haikou 570228, Hainan, China.*
† Electronic supplementary information (ESI) available.
‡ These authors contribute equally.

Materials

N, N-dimethylformamide (DMF), dimethyl sulfoxide (DMSO), chlorobenzene (CB), isopropanol (IPA) and $Pb(SCN)_2$ (99.9%) were purchased from Sigma-Aldrich. Anhydrous ethanol was purchased from Chengdu Chron Chemical Co., Ltd. Lead iodide (PbI_2, 99.99%) and lead bromide ($PbBr_2$, 99.99%), Cesium iodide (CsI, 99.999%) and bathocuproine (BCP, 99%) was purchased from TCI. Formamidinium iodide (FAI, 99.99%) was purchased from Advanced Election Technology Co., Ltd. NiOx NPs were synthesized according to a previously reported method.[1] 4PADCB was purchased from Shanghai Vizu Chemical Technology Co., Ltd. 1,3-propane-diammonium iodide (PDADI, 99.5%) was purchased from Xi'an Yuri Solar Co., Ltd. C_{60} was purchased from Nano-C. PTT, EDSA and AIBN (98%) were purchased from Energy Chemical Co., Ltd. Tetrakis (dimethylamino) tin (IV) (99.9999%) for atomic layer deposited (ALD) SnO_2 was bought from Nanjing Ai Mou Yuan Scientific Equipment. Indium tin oxide (ITO) (transmission>95%) substrates were purchased from Yingkou OPV Tech Co., Ltd. Cu was purchased from Zhongnuoxincai Co., Ltd. All the materials were used as received unless specified.

Device fabrication

Patterned indium tin oxide (ITO) glass substrates (25×25 mm, 10 Ω sq^{-1}) were sequentially cleaned with detergent, deionized water, and ethanol for 15 min at each procedure in an ultrasonic bath. Before the spin-coating of HTLs, ITO glass substrates were dried by a nitrogen flow and then treated with ultraviolet ozone for 15 min. NiOx films were formed on ITO by spin coating 20 mg NiOx in 1 mL deionized water at 4000 rpm for 30 s and then annealed at 120 ℃ for 20 min in air. 4PADCB was dissolved in anhydrous ethanol with a concentration of 0.5 mg/mL. The 4PADCB solution was spin-coated at 3000 rpm for 30 s and heated at 100 ℃ for 10 min.

The $FA_{0.8}Cs_{0.2}Pb(I_{0.6}Br_{0.4})_3$ perovskite precursor was prepared by dissolving 3.88 mg $Pb(SCN)_2$, 62.35 mg CsI, 165.12 mg FAI, 264.24 mg $PbBr_2$, 221.28 mg PbI_2 in 1 mL mixed solvent of DMF and DMSO with a volume ratio of 3:1 and stirred at 60 ℃ for 3 h before use. For the copoly-PE WBG perovskite, 1.3 mg PTT (0.3% molar ratio of Pb) and 1.7 mg EDSA (0.5% molar ratio of Pb) with 10 uL AIBN (2 mg/mL in DMF) (2% molar ratio of the total of PTT and EDSA) were added into 1 mL perovskite precursor. For the preparation of perovskite films, 80 μL of perovskite precursor was dropped on the substrate and spin-coated through a two-step process, 500 rpm for 2 s and then 4000 rpm for 60 s. At the second stage, 300 μL of

CB was dropped after the spin-coating of 25 s. The as-prepared perovskite film was annealed at 60 ℃ for 2 min and 100 ℃ for 10 min.

Then the perovskite films were treated by a PDADI solution dissolved in IPA with a concentration of 1 mg/mL at 3000 rpm for 30 s, and then followed by an additional annealing process at 100 ℃ for 10 min. After a short cooling, all samples were transferred into a thermal evaporation chamber, and a 20 nm C_{60} layer was evaporated at 5×10^{-4} Pa. For the opaque WBG devices, 5 nm BCP and 100 nm Cu were thermally evaporated in an evaporation chamber with a vacuum degree of 5×10^{-4} Pa. For the semi-transparent WBG devices, the deposition of ALD-SnO_2 was performed using tetrakis(dimethylamino) tin (IV) and deionized water as precursors for 20 nm. And, 100 nm IZO was sputtered at a 70 W power under Ar pressure of 0.3 Pa.

For the tandem devices, the semi-transparent WBG subcells were transferred to a glovebox for the fabrication of a 1.25 eV NBG subcell.[2] The active area of the device is 0.0975 cm^2, defined by the overlapped region between the back electrode and the patterned ITO substrate.

Device characterization

J-V curves were recorded by a Keysight Technologies B2901A source meter under simulated solar illumination (Enlitech, SS-F5-3A). The light intensity was calibrated by a silicon reference cell (SRC-00205, Enlitech). The scan rate for *J-V* measurement was 100 $mV\cdot s^{-1}$, with a delay time of 100 ms and a voltage step of 10 mV. The devices were tested using a shadow mask with an active area of 0.0576 cm^2. The light intensity dependence of V_{OC} was obtained by measuring *J-V* curves under different illumination intensities. The EQE spectra were measured under monochromatic light ranging from 300 nm to 800 nm with a chopper frequency of 210 Hz via a QE system (QE-R, Enli Tech). For tandem solar cells, EQE spectra were measured with two light-emitting diodes of 460 nm and 850 nm as the bias lights to measure WBG and NBG subcells. The MPP of the encapsulated devices were tracked by an LED (Guangzhou Crysco Equipment Co., Ltd.) under the relative humidity of ~ 50%. The light intensity was adjusted from 1 to 100 mW cm^{-2} to perform the light intensity dependence tests. EIS and C-V measurements were performed by an electrochemical workstation (IVIUMSTAT). For EIS measurement, the frequency was changed from 108 Hz to 1000 Hz at the bias of 1.1 V with an amplitude of 20 mV. For C-V measurement, the frequency was fixed at 1000 Hz with the voltage range of 0 V to 1.4 V. External electroluminescence quantum efficiency (EQE_{EL}) measurement was measured on ELCT-3010 (Enlitech) with a step of 0.1 V.

Film characterization

XPS measurements were carried out by XPS (Axis-Ultra DLD-600W). The IR spectra were recorded on a Bruker FT-IR spectrometer. AFM-IR experiments were carried out using a commercial AFM-IR setup (NanoIR3s, Bruker, CA, USA) that consists of an AFM microscope operating in contact mode and a Quantum Cascade Laser or QCL laser (MIRcat, Daylight Solutions Inc., CA, USA), that was tunable from 2350 cm^{-1} to 870 cm^{-1}. HR-TEM was performed on Talos F200X transmission electron microscope operated at 200 kV. For the samples preparation, a lower concentration of $FA_{0.8}Cs_{0.2}Pb(I_{0.6}Br_{0.4})_3$ perovskite precursor (0.5 mol/L) with or without copoly-PE was spin coated on ultra-thin carbon films. ToF-SIMS measurements was carried out using a ToF-SIMS 5 system from IONTOF, operated in the spectral mode and using a 30 keV Bi^{3+} primary ion beam. A field-emission SEM (FEI Nova NanoSEM450) was employed to measure the morphology patterns. The XRD spectra were measured by the X'pert PRO X-ray Diffractometer using Cu Kα radiation under operating conditions of 40 kV and 40 mA from 5° to 45°. GIXRD measurements were conducted using a Bruker D8 Advance (Cu Kα, 40 kV, 40 mA). UV–Vis optical absorption spectra were performed with an ultraviolet-visible spectrophotometer (PerkinElmer Lambda 950). The AFM and KPFM images were performed with Bruker Nano Inc DI Multi Mode 8. PL and TRPL measurements of perovskite films were performed by FLS980 (Edinburgh Inc) with a 532 nm wide spectrum light source as the excitation light source. TRPL mapping was obtained by laser confocal fluorescence lifetime imaging microscope FLIM300 (Timetechspectra Corporation) with an excitation at 532 nm.

Theoretical calculation method

All calculations were performed using the Vienna *ab initio* simulation package (VASP 6.1)[3, 4] with plane−wave pseudopotential method. The electronic exchange and correlation effects were described by the Perdew-Burke-Ernzerhof (PBE) functional with the generalized gradient approximation (GGA)[5] and the outermost s and p electrons were treated as valence electrons, whose interactions with the remaining ions were modelled by pseudopotentials generated within the projector-augmented wave (PAW) method.[6, 7] An energy cutoff of 500 eV for the plane-wave expansion was used and the energy and force convergence of 1×10^{-4} eV and 0.05 eV $Å^{-1}$, respectively. The 4×4×1 supercell was used for the $FAPbI_3$ slab model with 3 layers. For the sampling of the first Brillouin zone, we considered only the Γ point. To include the effect of the van der Waals (vdW) interaction, we performed structural relaxations with vdW dispersion−corrected functionals (DFT−D3) as implemented in VASP.[8] The visualization

of crystal structures was done using VESTA software.[9] Part of the post-processing was using VASPKIT.[10]

The binding energy is calculated as $E(\text{binding}) = E(\text{interface}) - E(\text{perovskite}) - E(\text{molecule})$, where E(interface) is the total energy of $FAPbI_3$ upon molecular passivation, and E(perovskite) and E(molecule) are the energies of isolated $FAPbI_3$ and PTT, EDSA, or copoly-PE.

Note S1.

To investigate the interactions of PTT and EDSA with Pb^{2+}, we employed X-ray photoelectron spectroscopy (XPS) to examine the chemical states of lead in perovskite films before and after adding PTT or EDSA (Fig. S1a). The binding energy at 138.34 eV (Pb $4f_{7/2}$) and 143.23 eV (Pb $4f_{5/2}$) were associated with the Pb^{2+} of the control perovskite sample. In comparison, the PTT modified film showed 0.2 eV shifted to lower binding energy, while the EDSA modified film showed 0.5 eV shift. These results indicated the decrease of the cationic charge of Pb^{2+} ions in perovskite films and the strong binding between EDSA and Pb^{2+}. Besides, compared with the control sample, the binding energy of Br 3d, and I 3d also decreased in PTT/EDSA modified films (Fig. S1b-c). The reduced anionic charges of under-bonded $Br^-$and I^- indicated that there were also interaction between Br^-/I^- and PTT/EDSA. In particular, EDSA has stronger interacting abilities due to its zwitterionic nature. Fourier transform infrared (FTIR) spectra showed a lower wavenumber (1721 cm^{-1}) for the PbI_2-PTT adduct than the bare PTT at 1725 cm^{-1} which contributed to C=O stretching vibration. For PbI_2-EDSA, the peak of S=O frequency was red-shifted from 1175 to 1168 cm^{-1} due to the binding of EDSA to PbI_2 through the O atom in the S=O bond (Fig. S2). This observation was consistent with the results of XPS.

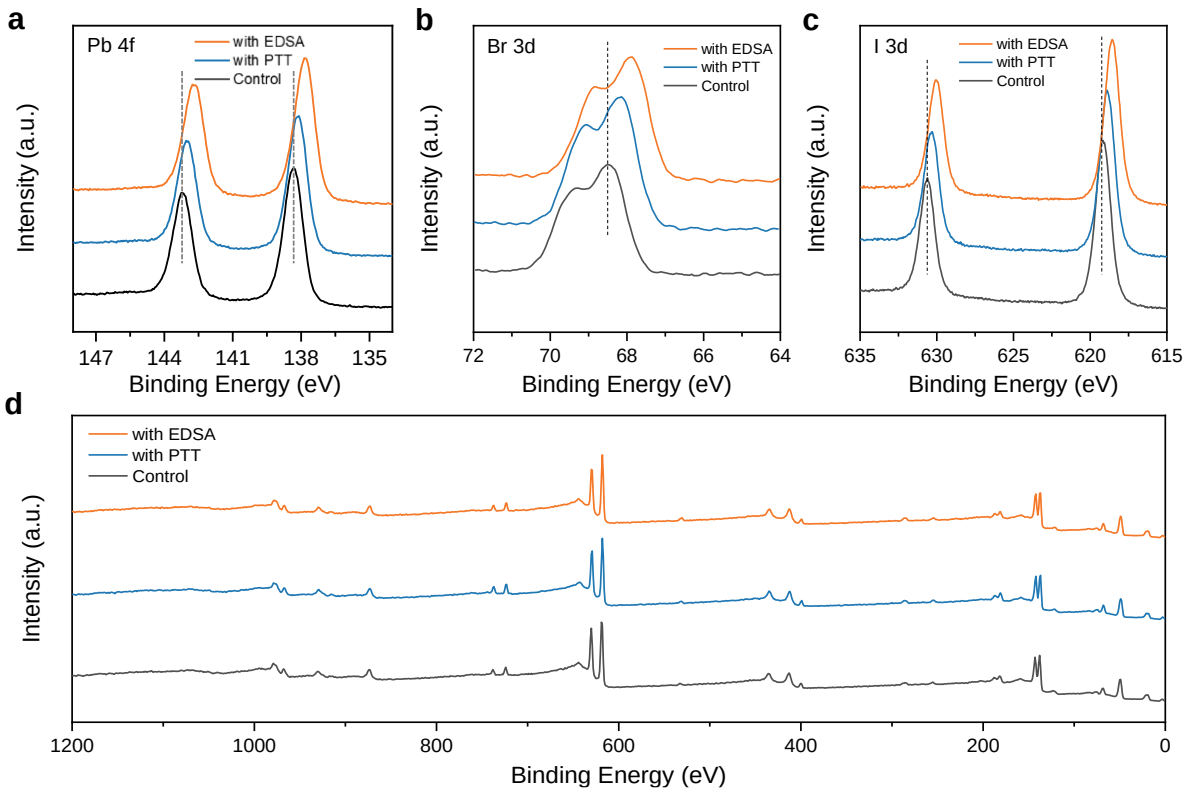

Fig. S1. The XPS spectra of (a) Pb 4f, (b) Br 3d, and (c) I 3d for control, PTT, and EDSA-modified perovskite films. (d) The full XPS spectra of control, PTT, and EDSA-modified perovskite films.

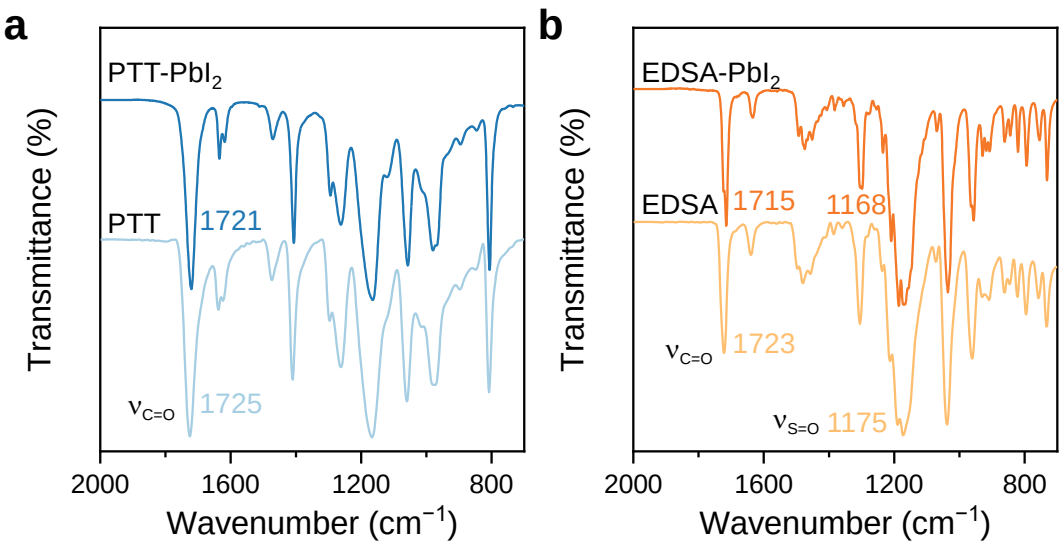

Fig. S2. (a) FTIR spectra of pure PTT and PTT-PbI_2. (b) FTIR spectra of pure EDSA and EDSA-PbI_2.

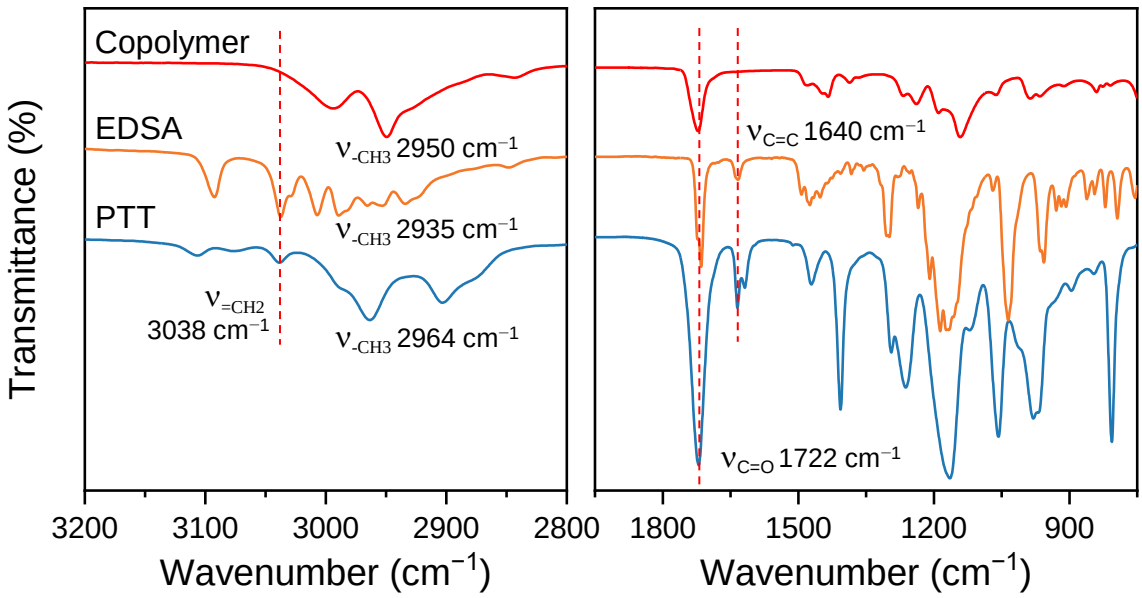

Fig. S3. FTIR spectra of the copolymer and its counterparts PTT, EDSA monomers.

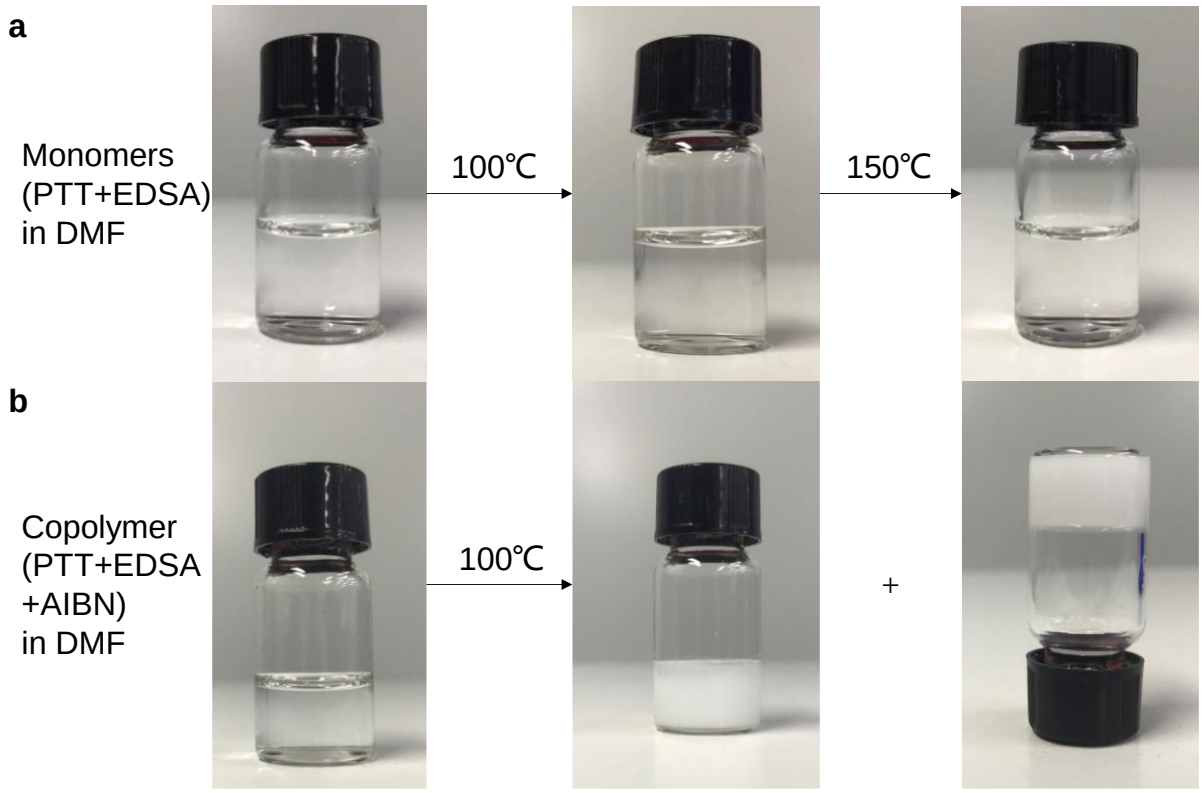

Fig. S4. Photographs of the copolymerization. (a) Photographs of PTT and EDSA (without AIBN) in reagent bottle before and after heating. PTT and EDSA were 20 mg/mL dissolved in DMF and always in liquid before and after heating. (b) Photographs of PTT and EDSA in reagent bottle before and after heating with initiator AIBN. After heated at 100 ℃, the liquid become a robust solid, indicating the cross-linking of PTT and EDSA.

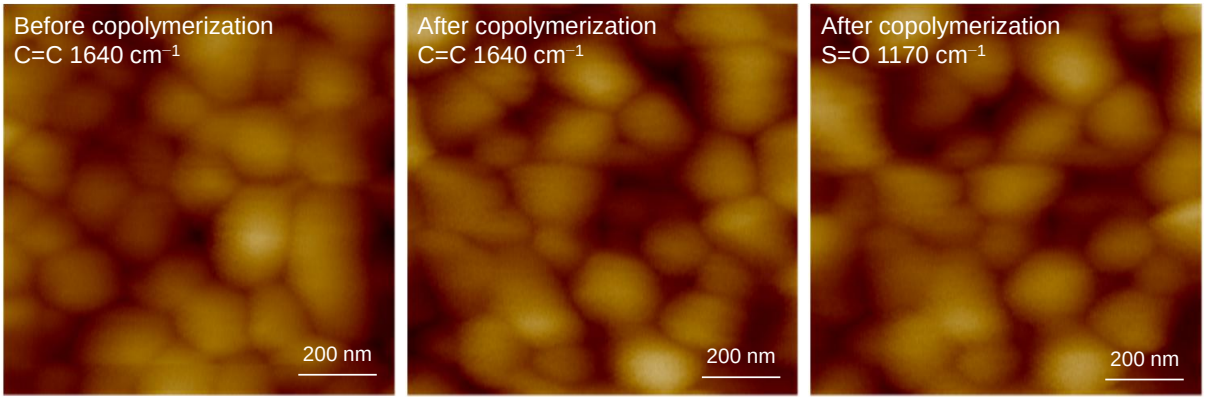

Fig. S5. AFM topography images corresponding to AFM-IR images.

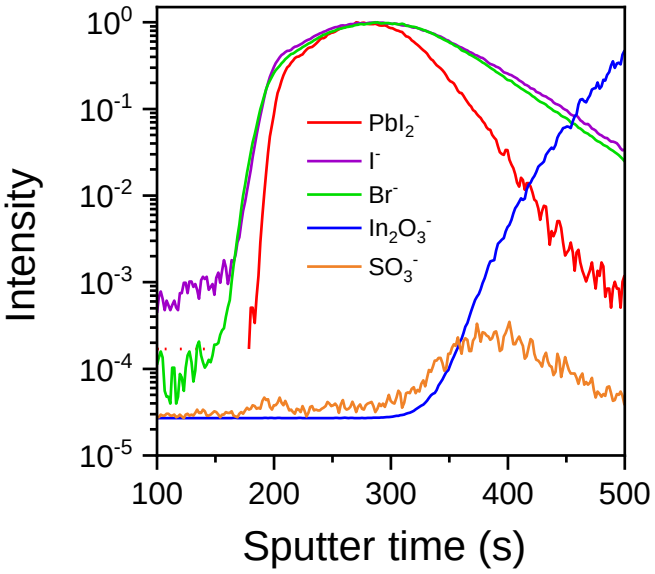

Fig. S6. ToF-SIMS results of copoly-PE device.

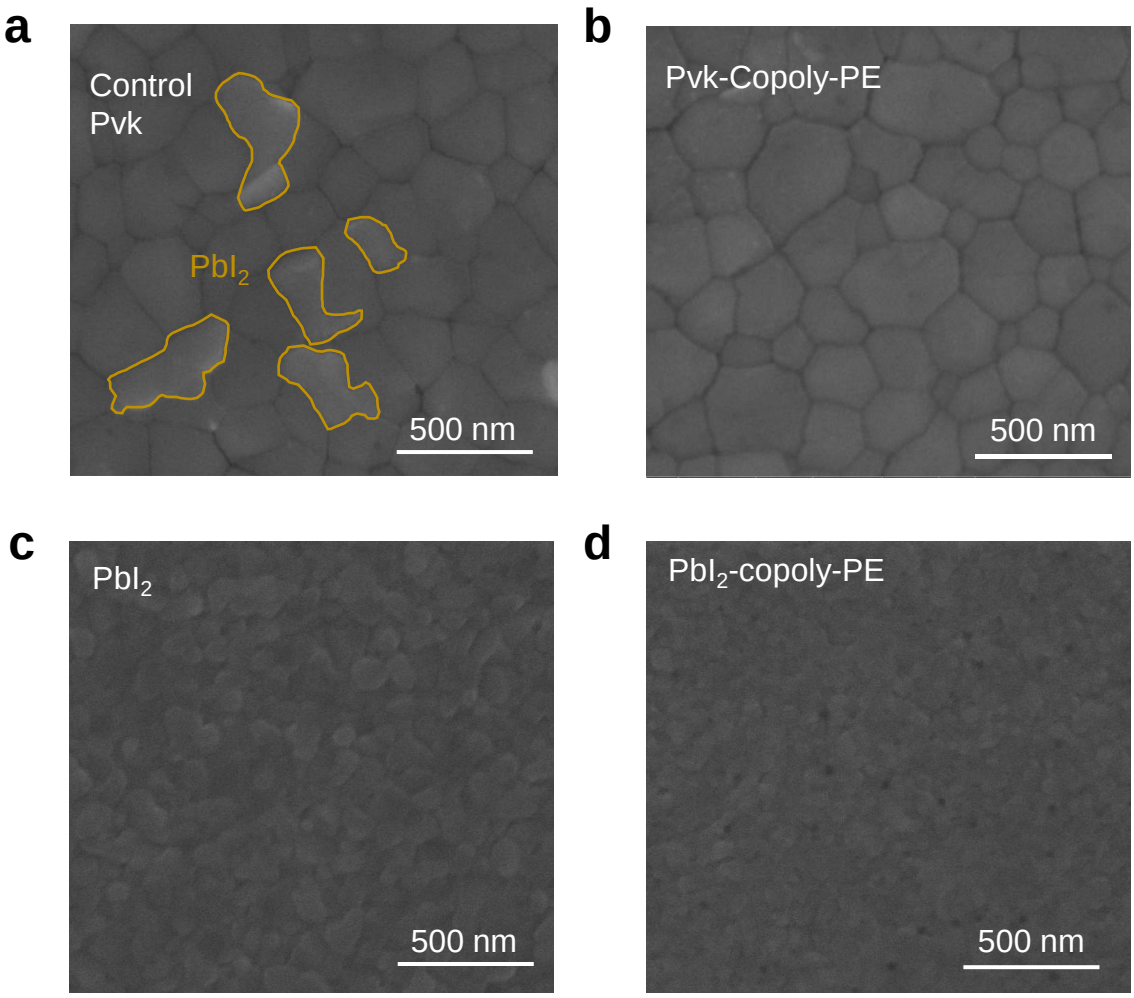

Fig. S7. Top-view SEM images of (a) control perovskite film, (b) copoly-PE film, (c) pristine PbI_2 film and (d) PbI_2-copoly-PE film.

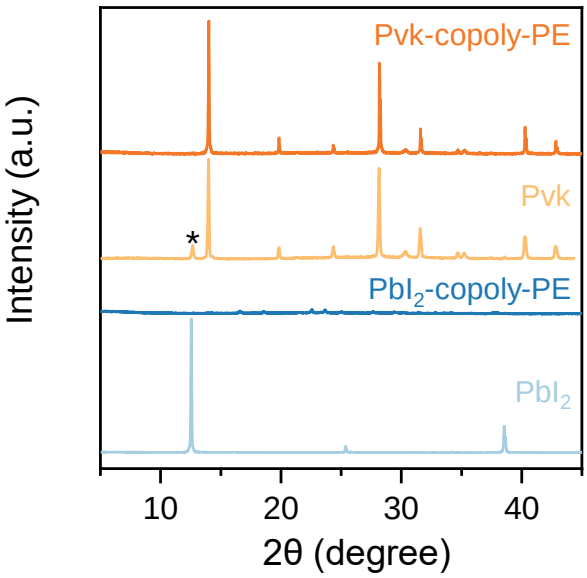

Fig. S8. XRD spectra of copoly-PE film and control perovskite film, PbI_2-copoly-PE film and pristine PbI_2 film.

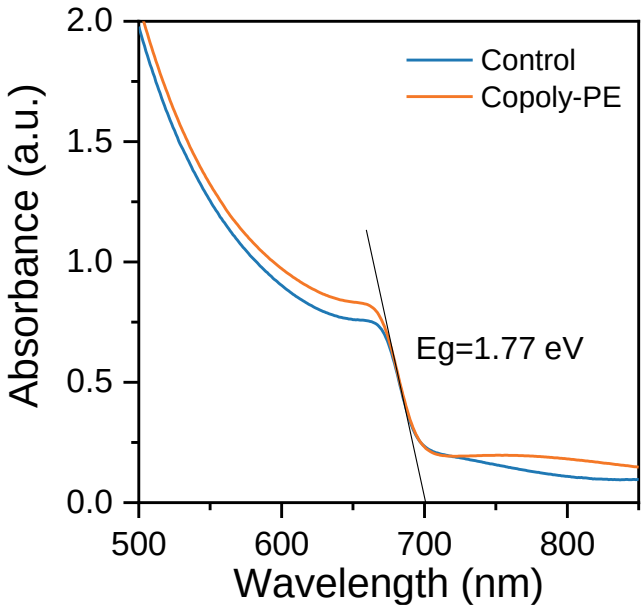

Fig. S9. UV-Vis spectra of the perovskite films with or without copoly-PE on ITO substrates.

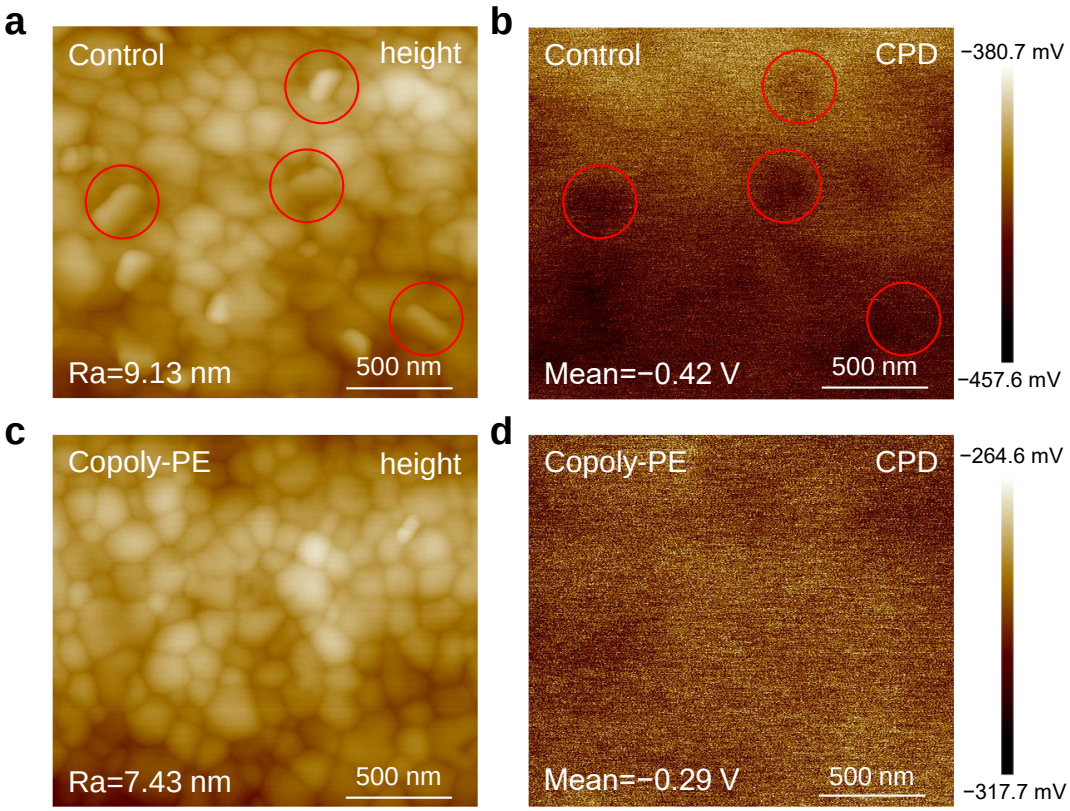

Fig. S10. AFM (Height) and KPFM (CPD) images of (a-b) control film and (c-d) copoly-PE film.

Note S2.

To study the roles of cross-linked polymers and co-polymers in suppressing light-induced phase segregation for perovskite films compared to their counterparts of small molecules and typical chain polymers, we measured the time-dependent PL spectra of the control (without additives), and the modified perovskite films by the following four additives.

(1) PTT monomer (a small molecule): the counterpart monomer of the copolymer copoly-PE, with no polymer formation.

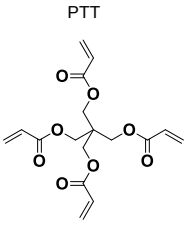

(2) chain polymer PMMA (obtained by introducing MMA + AIBN additives): it has a similar structure and functional group to PTT, but forms a chain polymer without network structure.

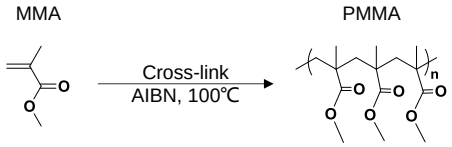

(3) cross-linked homopolymer poly-PTT (obtained by introducing PTT + AIBN additives): it is a homopolymer cross-linked polymer obtained from PTT polymerization, having a network structure but no other functional groups to passivate the defect of perovskite.

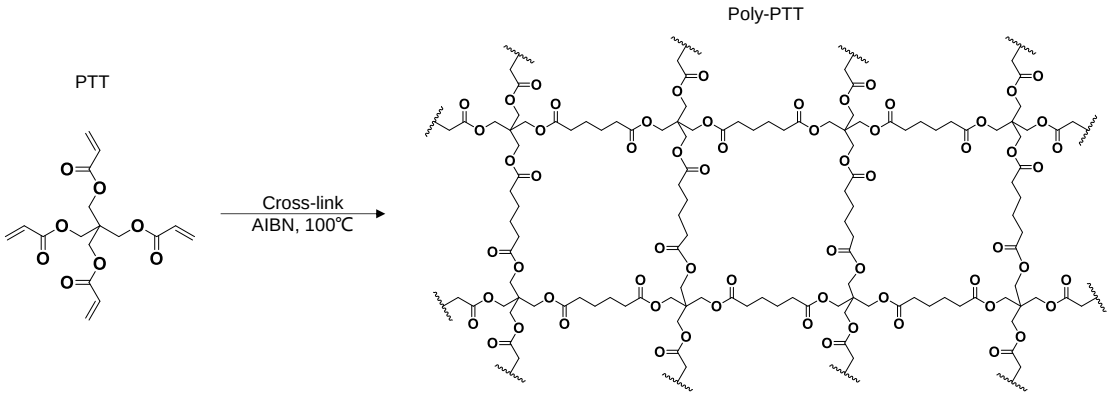

(4) cross-linked copolymer copoly-PE (obtained by introducing PTT + EDSA + AIBN additives): it is a cross-linked copolymer obtained from the copolymerization of PTT and EDSA, having a network structure and various types of functional groups that can interact with perovskite.

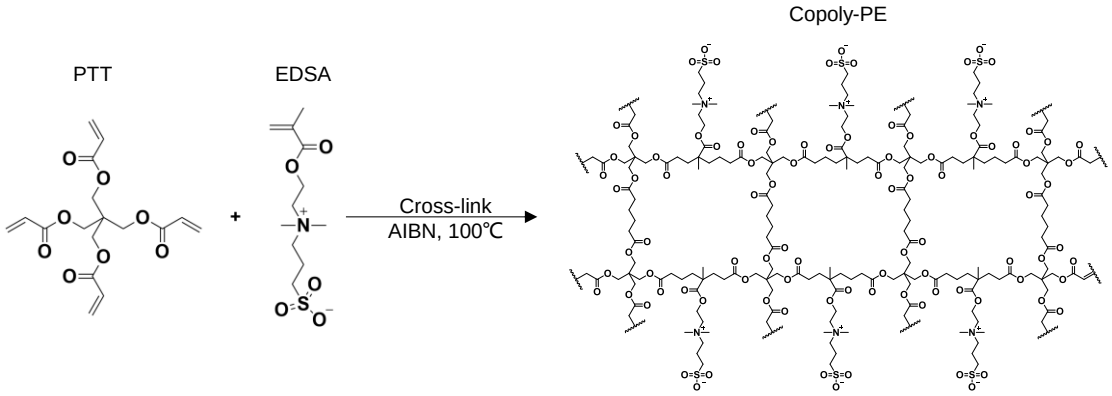

Samples preparation details:

(1) For the control perovskite film, the $FA_{0.8}Cs_{0.2}Pb(I_{0.6}Br_{0.4})_3$ perovskite precursor was deposited on glass.

(2) For the PTT film, 1.3 mg PTT (0.3% molar ratio of Pb) was added into 1 mL $FA_{0.8}Cs_{0.2}Pb(I_{0.6}Br_{0.4})_3$ perovskite precursor.

(3) For the PMMA film, 0.36 mg MMA (0.3% molar ratio of Pb) and 10 μL AIBN (2 mg/mL in DMF) (2% molar ratio of MMA) were added into 1 mL $FA_{0.8}Cs_{0.2}Pb(I_{0.6}Br_{0.4})_3$ perovskite precursor.

(4) For the poly-PTT film, 1.3 mg PTT (0.3% molar ratio of Pb) and 10 μL AIBN (2 mg/mL in DMF) (2% molar ratio of PTT) were added into 1 mL $FA_{0.8}Cs_{0.2}Pb(I_{0.6}Br_{0.4})_3$ perovskite precursor.

(5) For the copoly-PE film, 1.3 mg PTT (0.3% molar ratio of Pb) and 1.7 mg EDSA (0.5% molar ratio of Pb) with 10 μL AIBN (2 mg/mL in DMF) (2% molar ratio of the total of PTT and EDSA) were added into 1 mL $FA_{0.8}Cs_{0.2}Pb(I_{0.6}Br_{0.4})_3$ perovskite precursor.

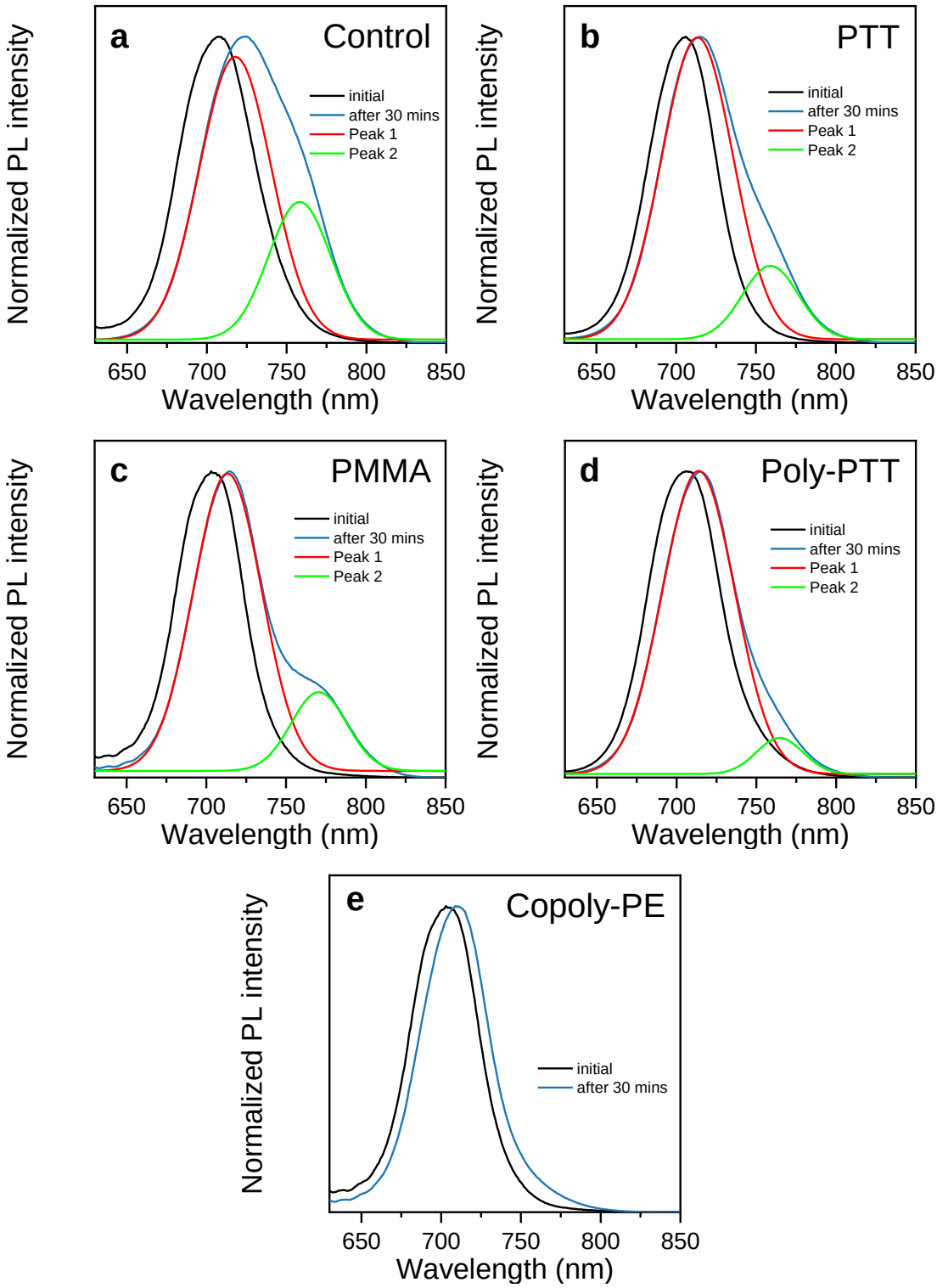

Fig. S11. Initial and after 30 min illumination PL spectra of (a) the control film, and the modified perovskite films by (b) PTT monomer, (c) chain polymer PMMA, (d) cross-linked homopolymer poly-PTT and (e) cross-linked copolymer copoly-PE, related to Fig. 2a-e.

Table S1. Initial PL peak and the PL spectra after illumination for 30 min and the fitting PL peaks of the control film, and the modified perovskite films by PTT, PMMA, poly-PTT and copoly-PE.

	control	PTT	PMMA	Poly-PTT	Copoly-PE
Initial peak	707 nm	706 nm	705 nm	706 nm	705 nm
Peak 1	719 nm	714 nm	714 nm	714 nm	710 nm
Peak 1 area ratio	70.3%	83.9%	82.4%	92.9%	100%
Peak 2	758 nm	759 nm	770 nm	764 nm	-
Peak 2 area ratio	29.7%	16.1%	17.6%	7.1%	-

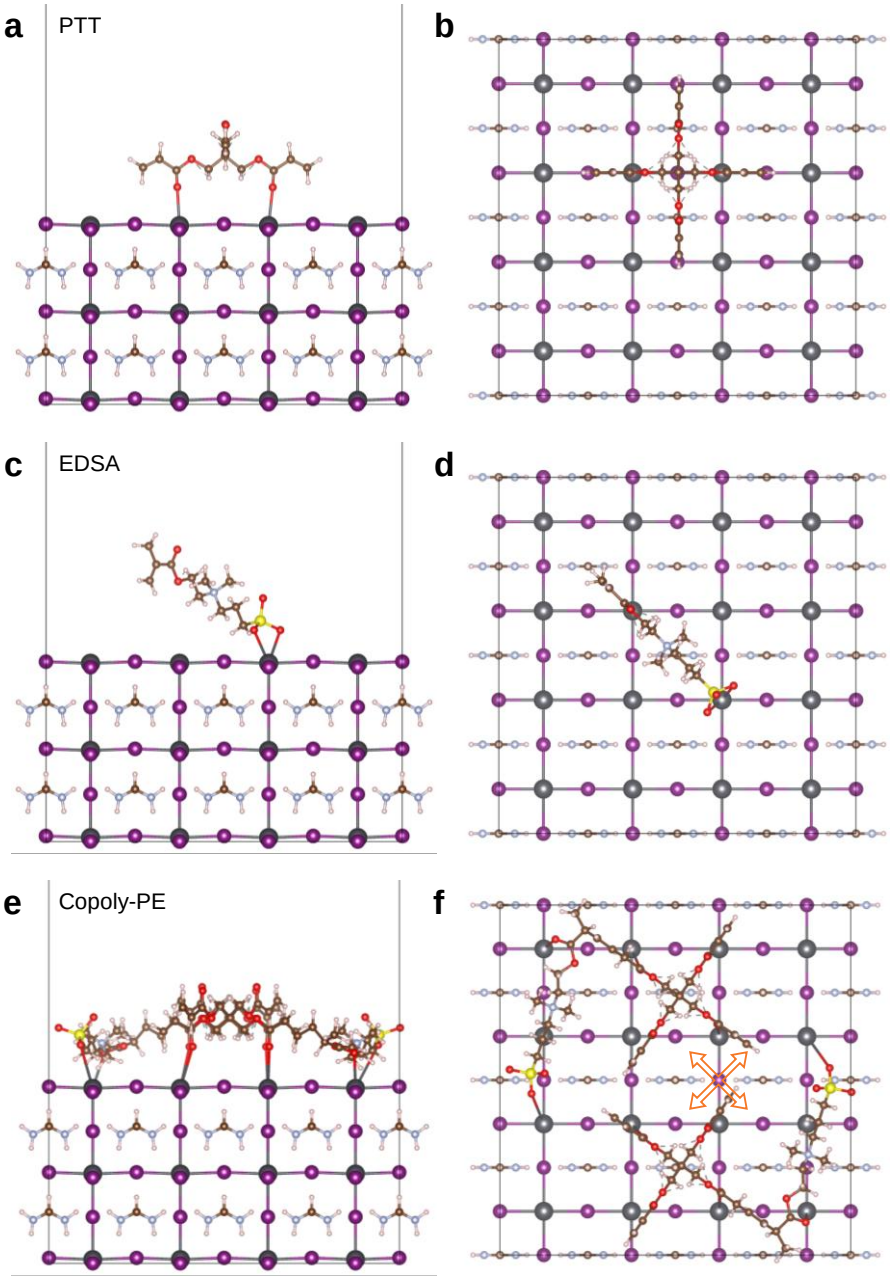

Fig. S12. (a-b) Side view and top view of EDSA-modified perovskite. (c-d) Side view and top view of PTT-modified perovskite. (e-f) Side view and top view of copoly-PE-modified perovskite. The arrow represented the diffusion path to its nearest site. The purple sphere represents an I atom, and the gray, cyan, brown, and white spheres represent Pb, N, C, and H atoms, respectively.

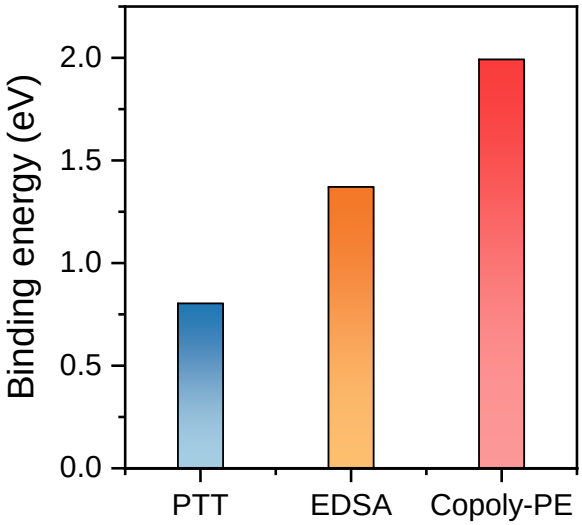

Fig. S13. The binding energies between perovskite GBs and PTT, EDSA, or copoly-PE.

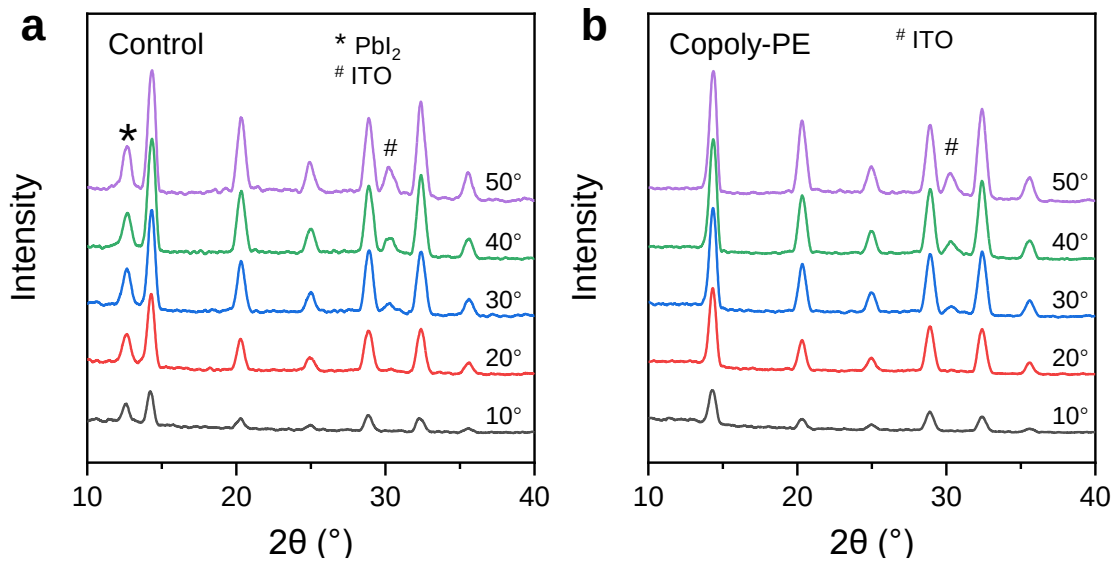

Fig. S14. GIXRD pattern at different tilt angles for (g) the control film and (h) copoly-PE film, respectively.

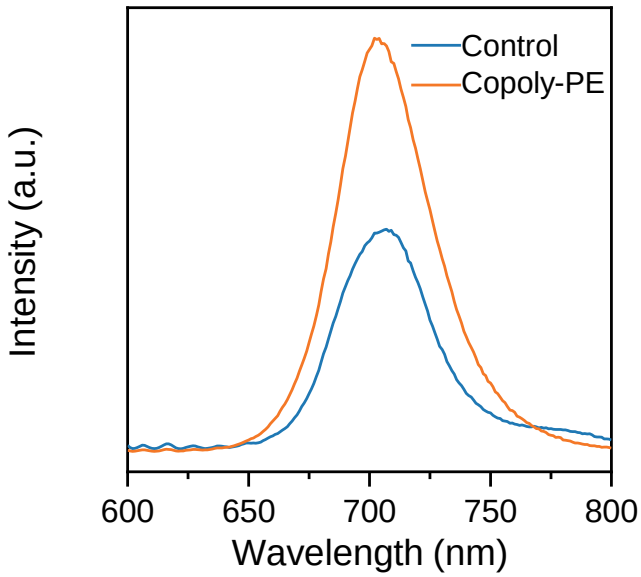

Fig. S15. Steady-state PL spectra on the glass substrates of control film and copoly-PE film.

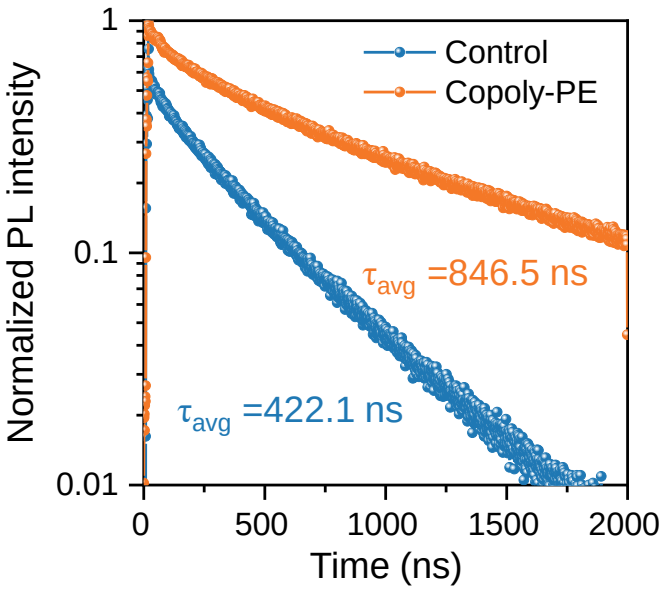

Fig. S16. TRPL decay profiles on glass substrates of control film and copoly-PE film.

Table S2. Carrier lifetimes obtained from TRPL spectra of perovskite films with and without copolymer treatment.

	A_1 (%)	τ_1 (ns)	A_2 (%)	τ_2 (ns)	τ_{avg} (ns)
Control	8.4	104.0	91.6	429.2	422.1
Copoly-PE	4.2	111.6	95.8	850.8	846.5

The average carrier lifetime is calculated with the equation of:

$$\tau_{avg} = (A_1\tau_1^2+A_2\tau_2^2)/(A_1\tau_1 + A_2\tau_2)$$

where the parameters A_1 and A_2 are the amplitude fraction for each decay component, and τ_1 and τ_2 represent the time constant of the two types of decay.

Note S3.

PLQY and QFLS calculation

According to Caprioglio et al.,[11] the quasi-Fermi levels $E_{F,e}$ and $E_{F,h}$ are quantities representing the density of the free photogenerated electron (holes) in the conduction (valence) band, in the limit of quasi-equilibrium. The difference between $E_{F,e}$ and $E_{F,h}$ is the QFLS, which can be determined directly by means of absolute PL measurements.

This method relies on the assumption, that all PL stems from the radiative recombination of free charges in the PVSK. Then, the quantum yield of the PL radiation is the ratio between the emitted photon flux φ_E from free carrier recombination on the PVSK and the absorbed photon flux φ_A or, equivalently, as the ratio between the total radiative recombination current J_{rad} and the generation current J_G, At V_{OC} conditions, the net current flowing in the device is zero and J_G is equal to the recombination current J_R, which consists in the radiative (J_{rad}) component and all non-radiative recombination processes ($J_{non\text{-}rad}$) in the PVSK and all other layers and interfaces and then we get the Equation S1.

$$\mathrm{PLQY} = \frac{\varphi_E}{\varphi_A} = \frac{J_{rad}}{J_G} = \frac{J_{rad}}{J_R} = \frac{J_{rad}}{J_{rad} + J_{non-rad}} \qquad (S1)$$

On the other hand, for quasi-equilibrium under steady state illumination, the density of free carriers in the valence and conduction band of the PVSK is related to the QFLS (or the sum of the chemical potentials of free electron-hole pair, μ) as follows:

$$n^2 = N_c N_v \cdot e^{\frac{E_c - E_v}{k_B T}} \cdot e^{\frac{E_{F,e} - E_{F,h}}{k_B T}} = {n_i}^2 \cdot e^{\frac{QFLS}{k_B T}} \qquad (S2)$$

where N_c and N_v are the effective density of states in the conduction band and the valence band respectively, T is the Kelvin temperature, k_B is the Boltzmann constant, q is the elementary charge. E_c and E_v are the conduction and valence band energy levels respectively, n_i is the intrinsic carrier density in the dark and QFLS represents the splitting of the quasi-Fermi levels. We relate now Equation S2 to the radiative recombination current $J_{rad} = edR = edkn^2$, which is the current originated exclusively from bimolecular radiative recombination in the PVK, and to the dark radiative recombination current $J_{0,rad} = edkn_i^2$, which is the current due to radiative

recombination of carriers in the dark. The latter is related to the absorption of the background black body radiation by the detailed balance principle.[12] Then:

$$J_{\mathrm{rad}} = J_{0,\mathrm{rad}} \cdot e^{\frac{\mathrm{QFLS}}{k_{\mathrm{B}}T}} \qquad (S3)$$

Combining with equation S1:

$$\mathrm{QFLS} = k_{\mathrm{B}}T \cdot ln\left(\mathrm{PLQY}\frac{J_{\mathrm{G}}}{J_{0,\mathrm{rad}}}\right) = k_{\mathrm{B}}T \cdot ln(\mathrm{PLQY}) + \mathrm{QFLS}_{\mathrm{rad}} \qquad (S4)$$

$\mathrm{QFLS}_{\mathrm{rad}}$ is the radiative limit of our semiconducting material, setting the maximum achievable splitting of the quasi-Fermi levels, hence the V_{OC}, in the case of zero nonradiative recombination.

Light-intensity dependent V_{OC} for the control and target devices

The diode ideality factor n is determined from the fitting of a semi-log plot of light intensity–dependent V_{OC} [$V_{OC} \sim (\ln I/I_0)$] to a linear dependence as according to:

$$V_{OC} = n\frac{k_B T}{q}\ln\left(\frac{I}{I_0}+1\right)$$

where k_B is the Boltzmann constant, T is the Kelvin temperature, q is the elementary charge. I is the light intensity, I_0 is a reference light intensity at one sun.

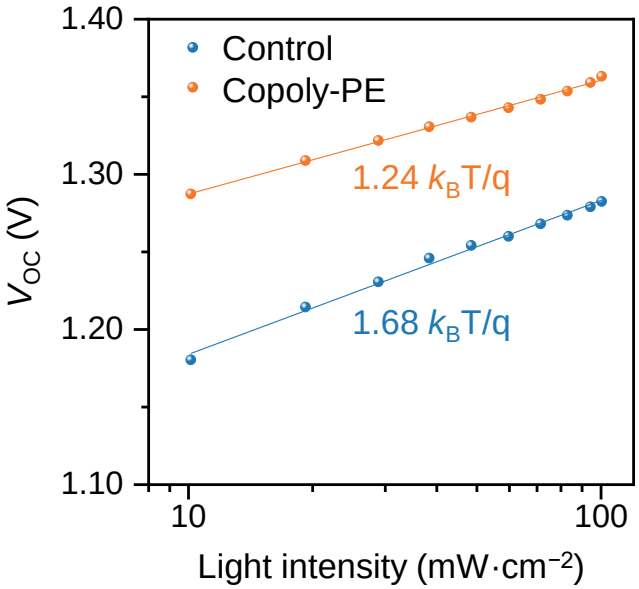

Fig. S17. V_{OC} dependence on light intensity of control and copoly-PE devices. The results were fitted with a linear function.

The calculation details of the trap state density in the perovskite by space-charge- limited current (SCLC) method

The trap states density N_t was determined by the trap filled limit voltage (V_{TFL}) using the following equation:

$$N_t = \frac{2\varepsilon\varepsilon_0}{eL^2} V_{TFL}$$

where e is the elementary charge, L is the thickness of the absorber film, ε_0 is the vacuum permittivity, and ε is the dielectric constant. It can be observed from the equation that V_{TFL} and N_t exhibit a direct proportional relationship.

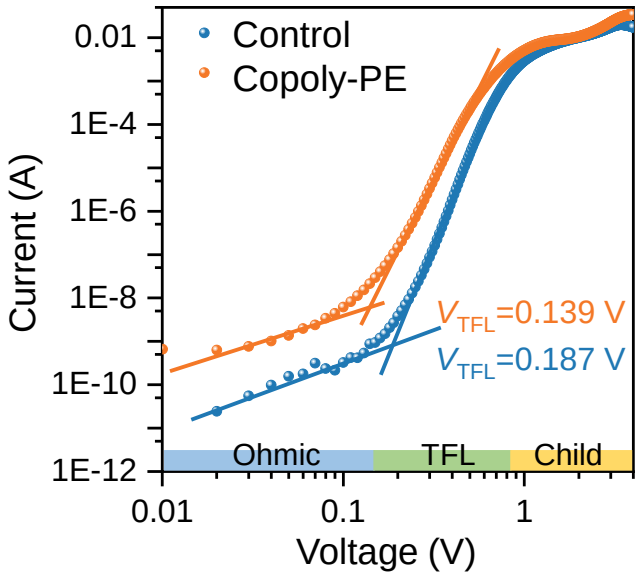

Fig. S18. SCLC measurements based on the electronic-only structure of ITO/SnO_2/perovskite/C_{60}/BCP/Cu.

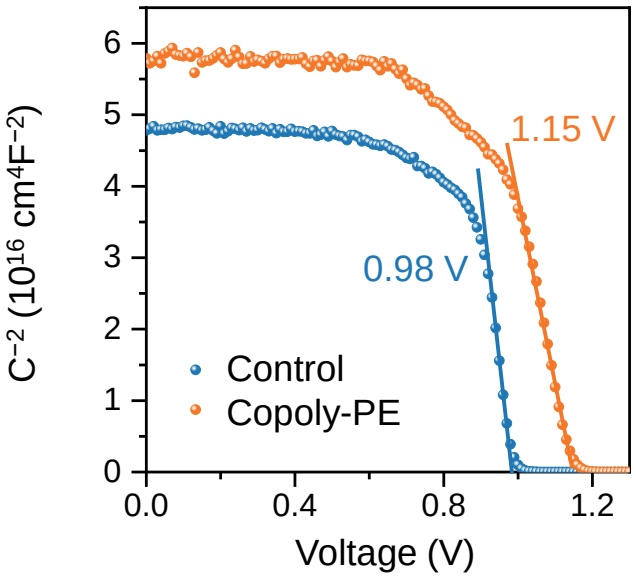

Fig. S19. Mott-Schottky plots of control and copoly-PE devices. The results in the rapid decline regions were fitted with a linear function.

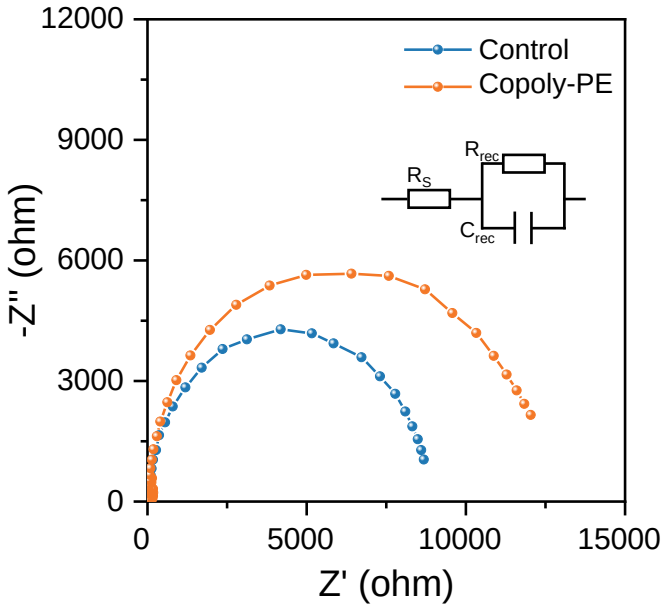

Fig. S20. Electrochemical impedance spectroscopy (EIS) plots of control and copoly-PE devices. The inset showed the corresponding equivalent circuit. The results were fitted with the equivalent circuit.

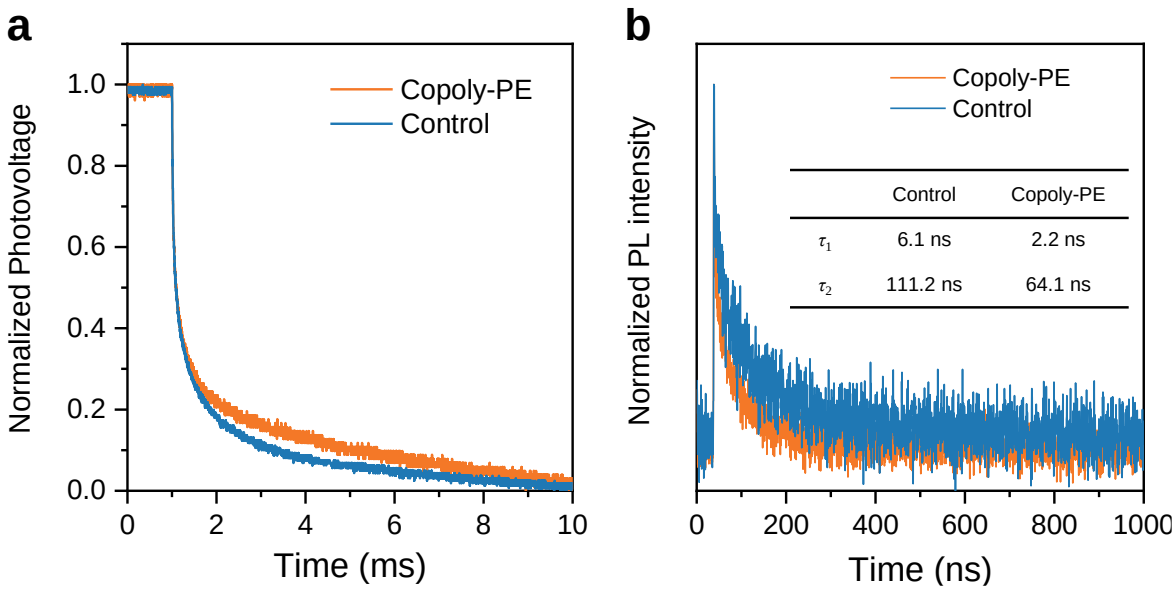

Fig. S21. (a) Transient photovoltage (TPV) decays of control and copoly-PE devices. (b) TRPL decay profiles on ITO substrates with ETL of control film and copoly-PE film.

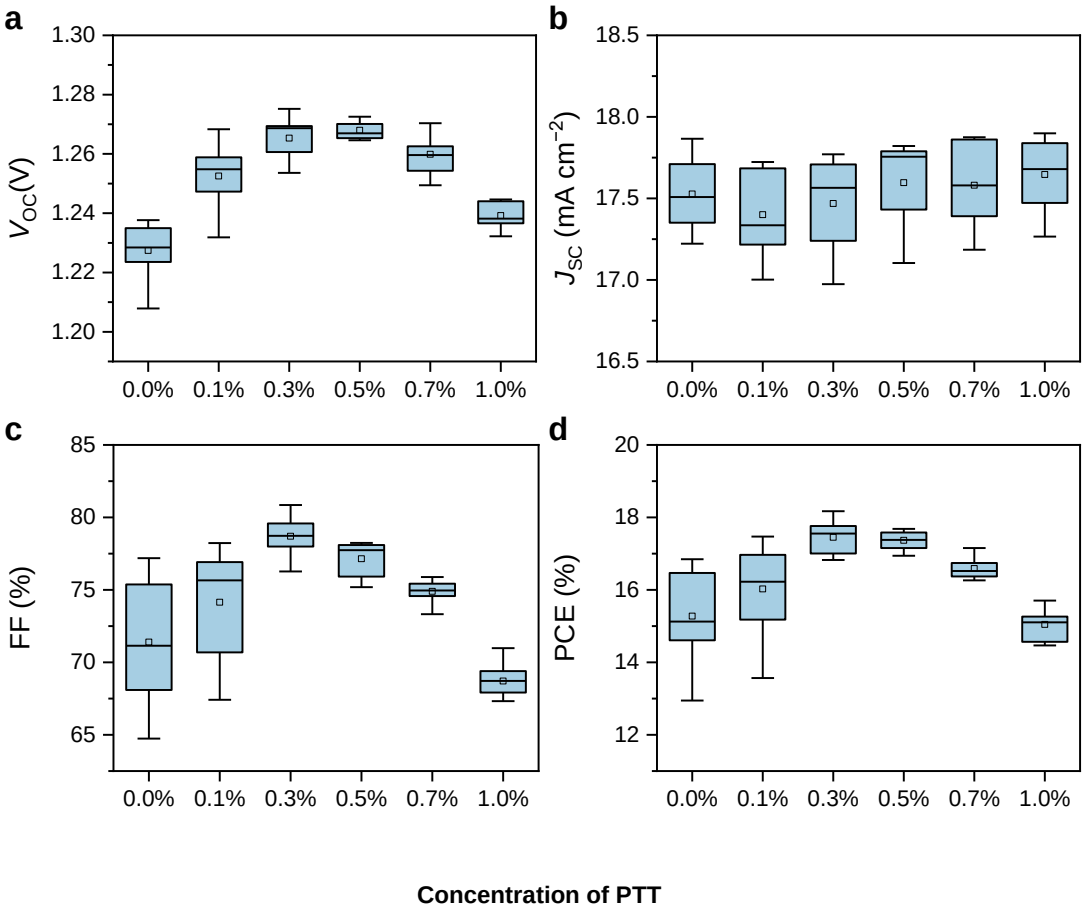

Fig. S22. The effect of PTT with different concentrations (0.1~1%) after polymerization on device performance. Statistics of photovoltaic parameters of WBG PSCs. Box charts of V_{OC} (a), J_{SC} (b), FF (c), and PCE (d). Sixteen devices were fabricated for each batch.

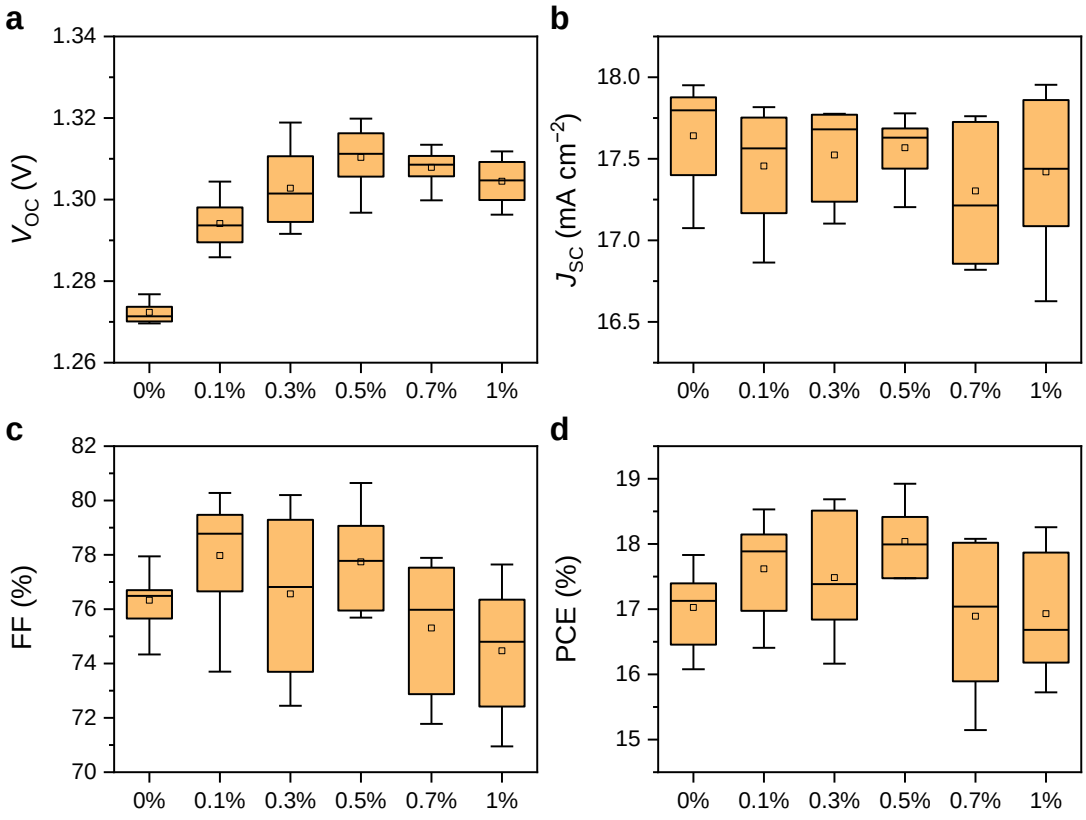

Fig. S23. The effect EDSA (0.1~1%) and PTT (0.3%) after polymerization on device performance. Statistics of photovoltaic parameters of WBG PSCs. Box charts of V_{OC} (a), J_{SC} (b), FF (c), and PCE (d). Sixteen devices were fabricated for each batch.

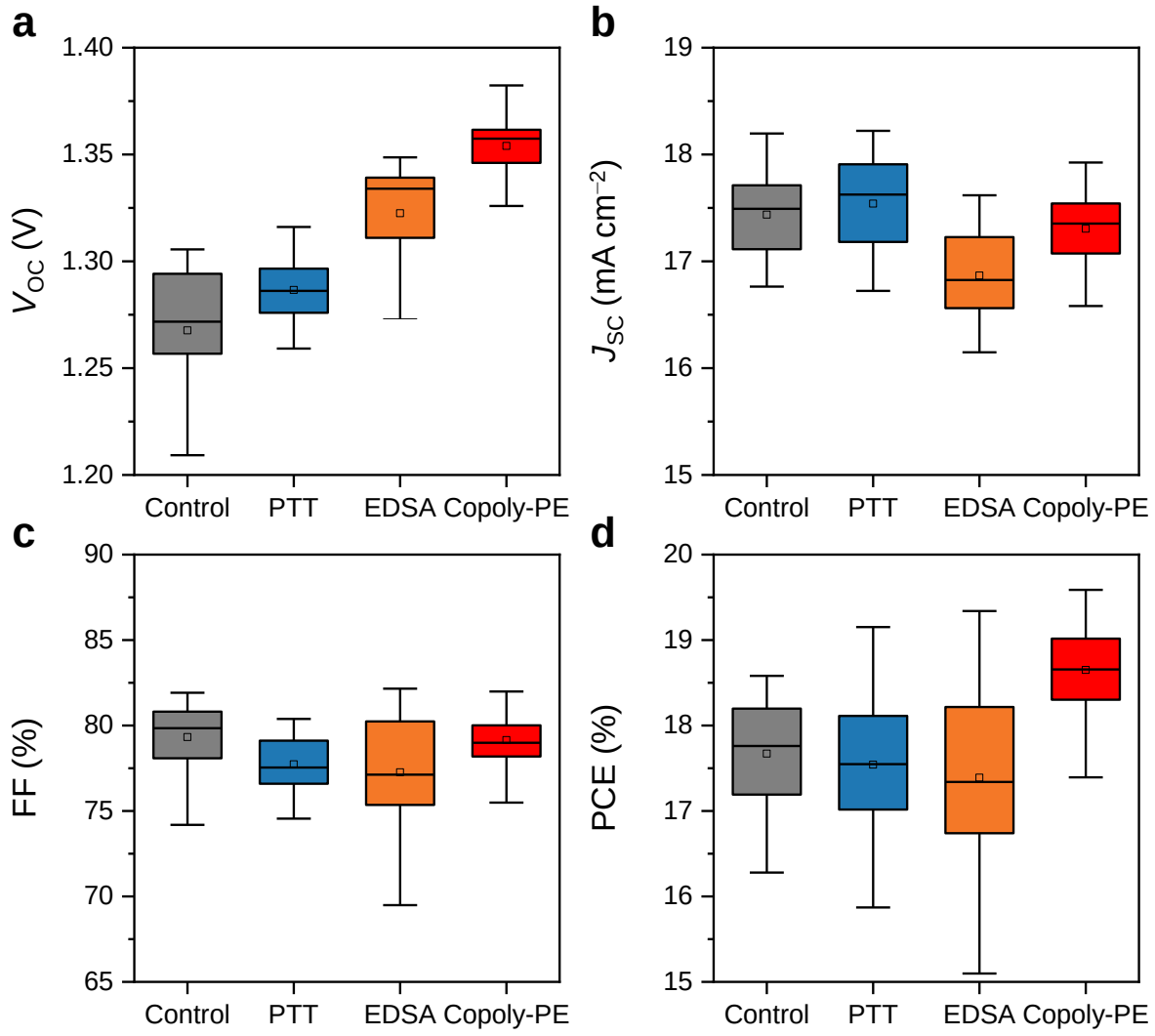

Fig. S24. The effect of PTT monomer, EDSA monomer and copoly-PE on device performance. Statistics of photovoltaic parameters of WBG PSCs. Box charts of V_{OC} (a), J_{SC} (b), FF (c), and PCE (d). Sixty devices were fabricated for each batch.

Fabrication details:

(1) For the PTT modified devices, 1.3 mg PTT (0.3% molar ratio of Pb) was added into 1 mL $FA_{0.8}Cs_{0.2}Pb(I_{0.6}Br_{0.4})_3$ perovskite precursor.

(2) For the EDSA modified devices, 1.7 mg EDSA (0.5% molar ratio of Pb) was added into 1 mL $FA_{0.8}Cs_{0.2}Pb(I_{0.6}Br_{0.4})_3$ perovskite precursor.

(3) For the copoly-PE modified devices, 1.3 mg PTT (0.3% molar ratio of Pb) and 1.7 mg EDSA (0.5% molar ratio of Pb) with 10 μL AIBN (2 mg/mL in DMF) (2% molar ratio of the total of PTT and EDSA) were added into 1 mL $FA_{0.8}Cs_{0.2}Pb(I_{0.6}Br_{0.4})_3$perovskite precursor.

Table S3. Summary of the photovoltaic parameters of the control devices and copoly-PE WBG devices.

	Scan direction	V_{OC} (V)	J_{SC} (mA cm^{-2})	FF (%)	PCE (%)
Control WBG devices	Forward	1.30 (1.27±0.03)	17.5 (17.3±0.4)	79.9 (78.1±1.9)	18.2 (17.3±0.8)
	Reverse	1.30 (1.27±0.03)	17.5 (17.4±0.4)	81.3 (79.3±1.9)	18.5 (17.7±0.6)
Copoly-PE WBG devices	Forward	1.36 (1.35±0.01)	17.5 (17.3±0.4)	79.3 (78.1±1.7)	18.9 (17.9±0.7)
	Reverse	1.36 (1.35±0.01)	17.5 (17.3±0.3)	82.0 (80.1±1.5)	19.5 (18.8±0.5)

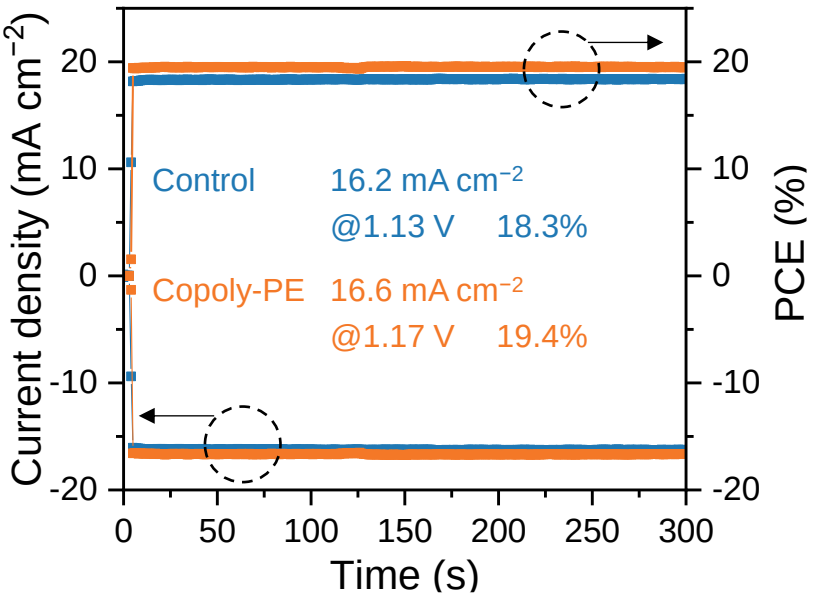

Fig. S25. Stabilized power output (SPO) of the control and copoly-PE devices.

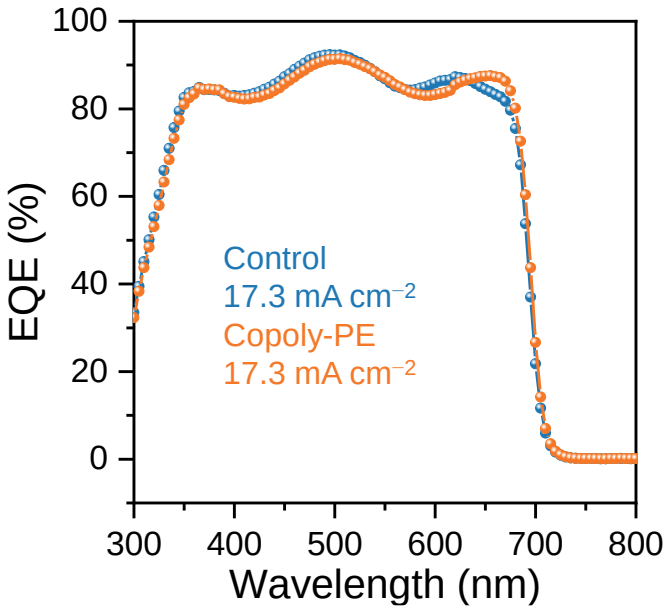

Fig. S26. EQE curves for the control and copoly-PE WBG PSCs.

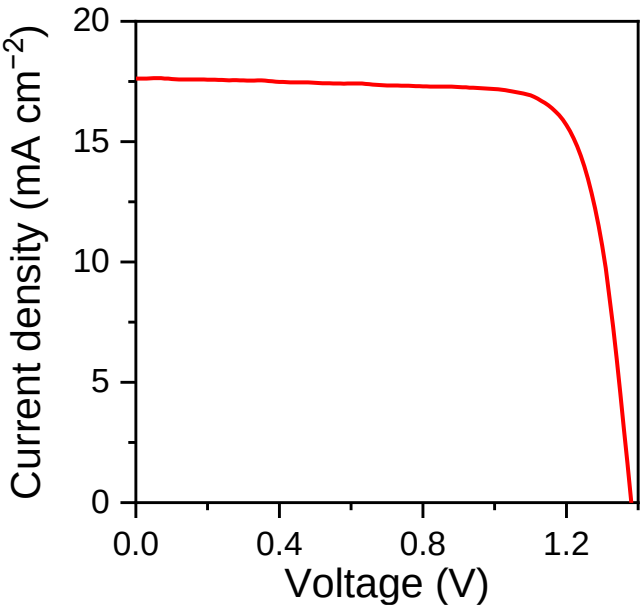

Fig. S27. *J*–*V* curves of the champion V_{OC} device.

Champion V_{OC} device	V_{OC} (V)	J_{SC} (mA cm^{-2})	FF (%)	PCE (%)
Reverse	1.38	17.6	78.2	19.0

Table S4. Summary of the photovoltaic parameters of WBG (1.75 -1.8 eV) PSCs extracted from recent literature on all-perovskite TSCs.

Bandgap (eV)	V_{OC} (V)	J_{SC} (mA cm^{-2})	FF (%)	PCE (%)	Ref.
1.76	1.14	-	-	14.6	[13]
1.76	1.22	17.4	81.6	17.3	[14]
1.77	1.23	17.0	79.8	16.7	[15]
1.75	1.24	17.92	81.9	18.19	[16]
1.75	1.24	16.5	69.4	14.2	[17]
1.77	1.25	17.2	80.0	17.4	[18]
1.75	1.26	18.12	80	18.3	[19]
1.79	1.26	16.94	80.17	17.04	[20]
1.79	1.26	17.90	78.9	17.80	[21]
1.77	1.26	18.5	76.5	17.8	[22]
1.80	1.263	17.4	79.7	17.7	[23]
1.78	1.274	17.7	82.6	18.6	[24]
1.77	1.284	17.19	80.29	17.72	[25]
1.77	1.286	17.54	82.61	18.63	[26]
1.77	1.29	15.0	77.9	15.1	[27]
1.75	1.29	18.0	84.8	19.7	champion[28]
1.75	1.273	18.18	81.26	18.81	certified[28]
1.77	1.31	17.93	82.31	19.33	champion[29]
1.77	1.291	17.91	82.25	19.09	certified[29]
1.73	1.312	18.89	81.6	20.22	[30]
1.75	1.32	18.7	82.2	20.3	[31]
1.79	1.33	18.06	84.2	20.2	champion[32]
1.79	1.33	17.3	83.9	19.3	certified[32]
1.77	1.33	17.75	82.70	19.53	champion[33]
1.77	1.339	16.65	84.65	18.88	certified[33]
1.80	1.34	18.2	83.9	20.3	[34]
1.78	1.36	17.53	82.76	19.83	[35]
1.77	1.38	17.6	78.2	19.0	This work
	1.36	17.5	82.0	19.5	This work
	1.37	15.3	82.2	17.2	Certified

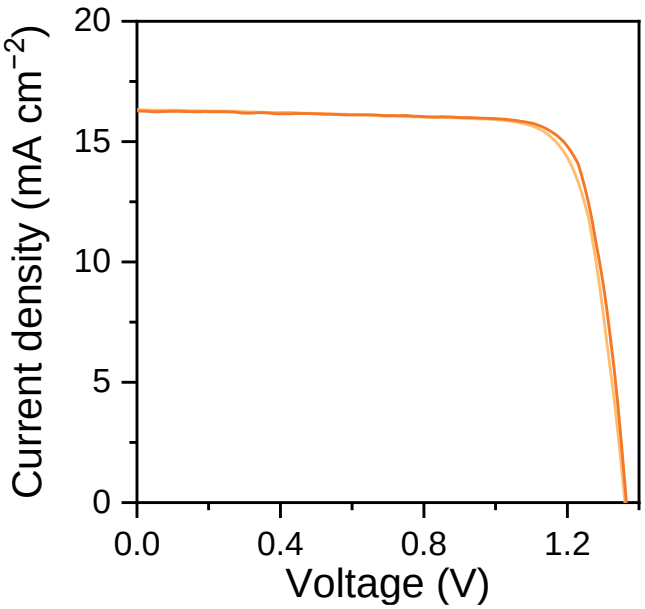

Fig. S28. *J–V* curves of the IZO device with the device structure of ITO/NiO_x/4PADCB/perovskite/C_{60}/ALD-SnO_2/IZO.

IZO device	V_{OC} (V)	J_{SC} (mA cm^{-2})	FF (%)	PCE (%)
Forward	1.36	16.3	79.2	17.6
Reverse	1.37	16.3	80.2	17.9

230017163974

中国认可
国际互认
检测
TESTING
CNAS L8490

Test and Calibration Center of New Energy Device and Module,
Shanghai Institute of Microsystem and Information Technology,
Chinese Academy of Sciences (SIMIT)

Measurement Report

Report No. 23TR082001

Client Name	Huazhong University of Science and Technology
Client Address	1037 Luoyu Road, Wuhan, 430074, P. R. China
Sample	Perovskite Solar Cell
Manufacturer	Wuhan Photoelectric National Research Center
Measurement Date	21th August, 2023

Performed by:	Qiang Shi	**Date:** 21/08/2023
Reviewed by:	Wenjie Zhao	**Date:** 21/08/2023
Approved by:	Zhengxin Liu	**Date:** 21/08/2023

Address: No.235 Chengbei Road, Jiading, Shanghai **Post Code:**201800

E-mail: solarcell@mail.sim.ac.cn **Tel:** +86-021-69976921

Sample Information	
Sample Type	Perovskite Solar Cell
Serial No.	5-1#
Lab Internal No.	23082001-1#
Measurement Item	I-V characteristic
Measurement Environment	24.8±1.0°C, 46.4±5.0%R.H

Measurement of I-V characteristic	
Reference cell	PVM1121
Reference cell Type	mono-Si, WPVS, calibrated by NREL (Certificate No. ISO 2075)
Calibration Value/Date of Calibration for Reference cell	144.53mA/ Feb. 2023
Measurement Conditions	Standard Test Condition (STC): Spectral Distribution: AM1.5 according to IEC 60904-3 Ed.3, Irradiance: 1000±50W/m², Temperature: 25±2°C
Measurement Equipment/ Date of Calibration	AAA Steady State Solar Simulator (YSS-T155-2M) / July.2022 IV tester (ADCMT 6243) / Apr. 2023 Measuring Microscope (MF-B2017C) / July.2022
Measurement Method	I-V Measurement: Irradiance adjusted to 1000W/m² according to the short circuit current value of calibrated reference cell; Logarithmic sweep in both directions (Isc to Voc and Voc to Isc) during one flash based on IEC 60904-1:2020;
Measurement Uncertainty	Area: 1.0%(k=2); Isc: 2.2%(k=2); Voc: 1.0%(k=2); Pmax: 2.5%(k=2); Eff: 2.7%(k=2)

Report No. 23TR082001

====Measurement Results ====

	Forward Scan (Isc to Voc)	Reverse Scan (Voc to Isc)
Area	6.25 mm^2	
Isc	0.949 mA	0.955 mA
Voc	1.359 V	1.367 V
Pmax	1.032 mW	1.073 mW
Ipm	0.876 mA	0.901 mA
Vpm	1.178 V	1.191 V
FF	79.99 %	82.23 %
Eff	16.51 %	17.17 %

- Designated illumination area defined by a mask was measured by a measuring microscope.
- Test results listed in this measurement report refer exclusively to the mentioned test sample.
- The results apply only at the time of the test, and do not imply future performance.

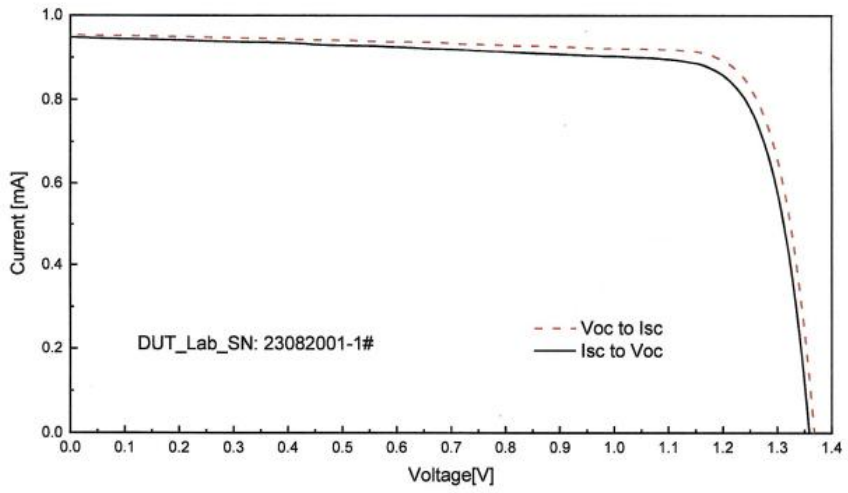

Fig.1 I-V curves of the measured sample

-------End of Report-------

3 / 3

Fig. S29. Measurement report of a WBG PSC certified by Shanghai Institute of Microsystem and Information Technology. The device had an independently certified V_{OC} of 1.367 V (1.359 V) and PCE of 17.17% (16.51%) under reverse (forward) voltage scan.

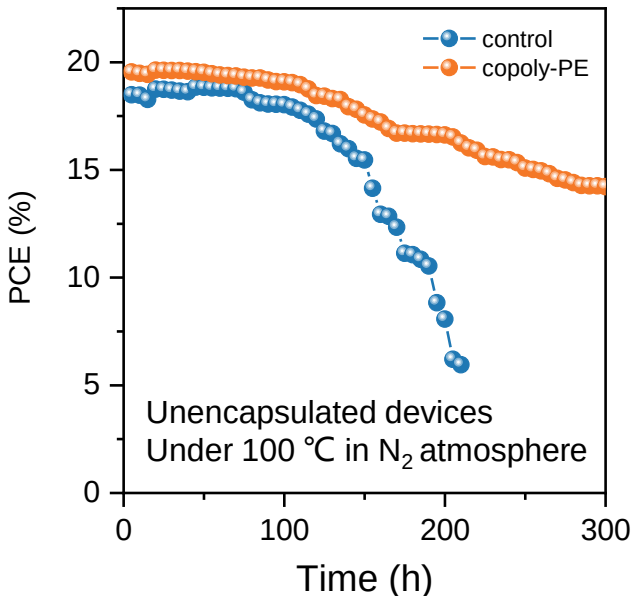

Fig. S30. Continuous thermal aging of the control and copoly-PE devices without encapsulation at 100 ℃ in a N_2-filled glovebox.

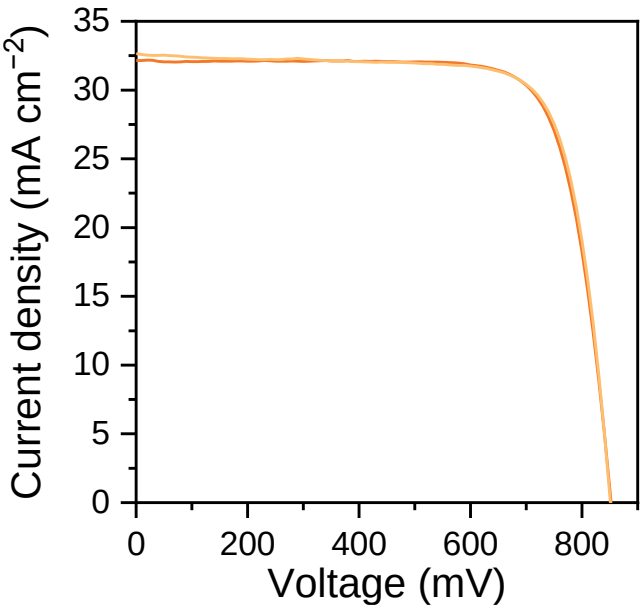

Fig. S31. Photovoltaic performance of NBG device. *J*-*V* curves under forward and reverse voltage scans.

NBG	V_{OC} (V)	J_{SC} (mA cm^{-2})	FF (%)	PCE (%)
Forward	0.851	32.6	76.9	21.3
Reverse	0.852	32.2	77.6	21.3

Table S5. Summary of the photovoltaic parameters of the control devices and copoly-PE tandem devices.

	Scan direction	V_{OC} (V)	J_{SC} (mA cm^{-2})	FF (%)	PCE (%)
Control tandem devices	Reverse	2.10 (2.08±0.04)	15.8 (15.5±0.4)	80.6 (79.3±2.8)	26.7 (25.7±1.3)
Copoly-PE tandem devices	Reverse	2.17 (2.14±0.03)	16.1 (15.7±0.3)	81.2 (79.8±1.5)	28.3 (26.8±0.5)

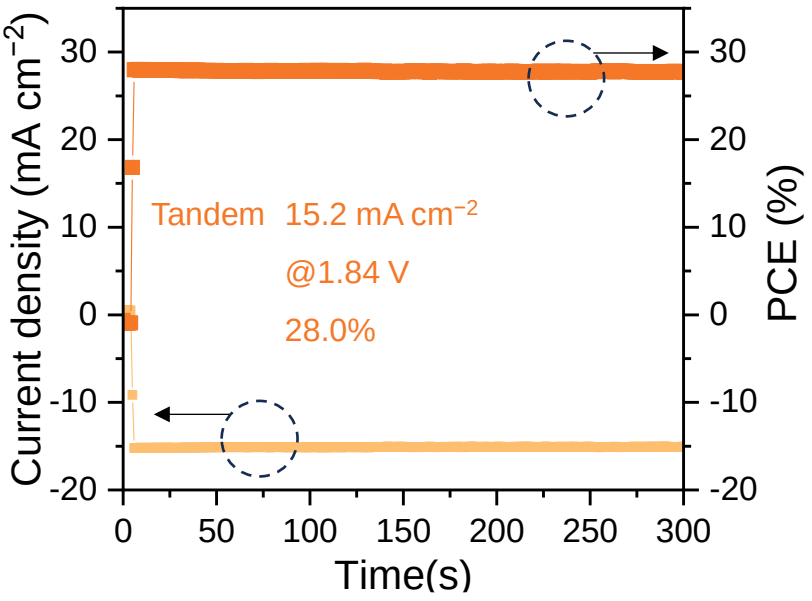

Fig. S32. Stabilized power output (SPO) of the best-performing all-perovskite tandem cell.

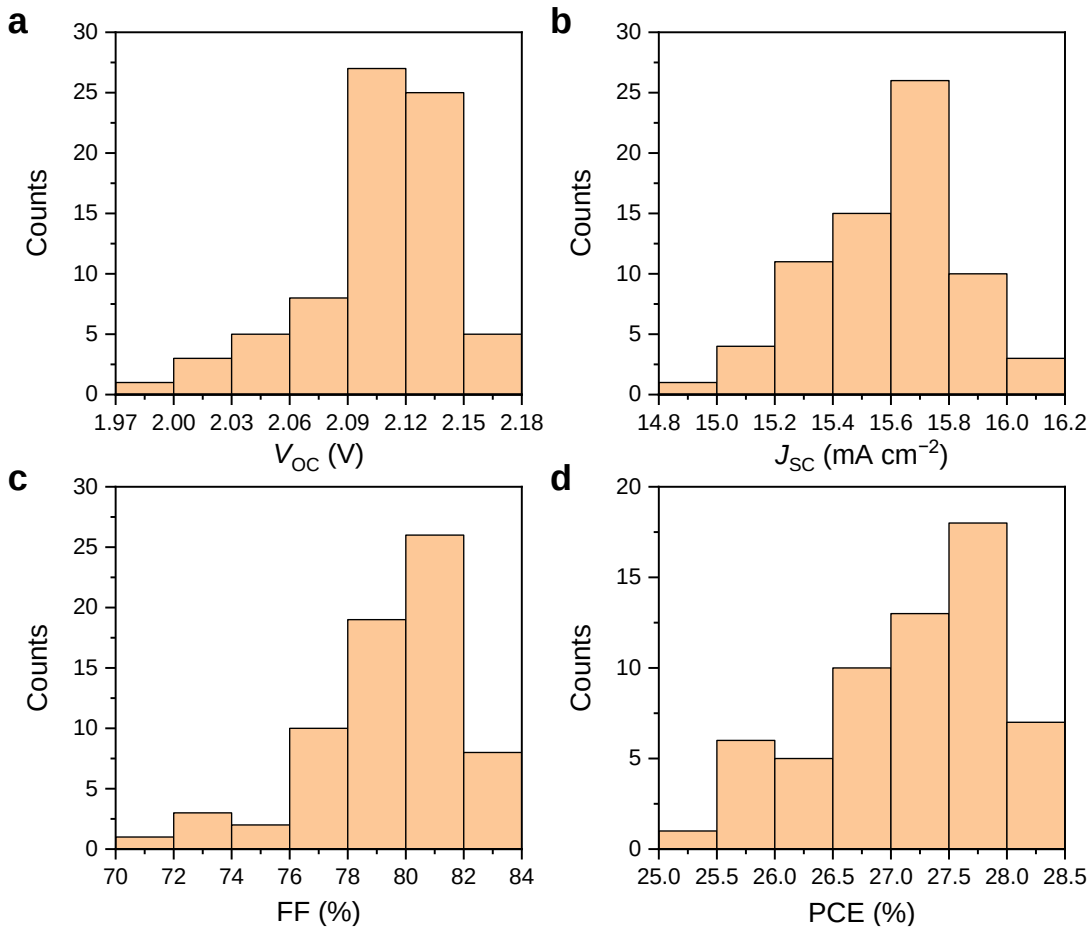

Fig. S33. V_{OC} (a), J_{SC} (b), FF(c), and PCE (d) histograms of 70 tandem cells.

References

1. W. Chen, Y. Zhou, L. Wang, Y. Wu, B. Tu, B. Yu, F. Liu, H. W. Tam, G. Wang, A. B. Djurišić, L. Huang and Z. He, *Adv. Mater.*, 2018, **30**, 201800515.
2. J. Zhu, Y. Xu, Y. Luo, J. Luo, R. He, C. Wang, Y. Wang, K. Wei, Z. Yi, Z. Gao, J. Wang, J. You, Z. Zhang, H. Lai, S. Ren, X. Liu, C. Xiao, C. Chen, J. Zhang, F. Fu and D. Zhao, *Sci. Adv.*, 2024, **10**, eadl2063.
3. G. Kresse and J. Hafner, *Phys. Rev. B*, 1993, **47**, 558-561.
4. G. Kresse and J. Furthmüller, *Phys. Rev. B*, 1996, **54**, 11169–11186.
5. John P. Perdew, Kieron Burke and M. Ernzerhof, *Phys. Rev. Lett.*, 1996, **77**, 3865–3868.
6. P. E. Blöchl, *Phys. Rev. B*, 1994, **50**, 17953-17979.
7. G. Kresse and D. Joubert, *Phys. Rev. B*, 1999, **59**, 1758–1775.
8. S. Grimme, J. Antony, S. Ehrlich and H. Krieg, *J. Chem. Phys.*, 2010, **132**.
9. K. Momma and F. Izumi, *J. Appl. Crystallogr.*, 2011, **44**, 1272-1276.
10. V. Wang, N. Xu, J.-C. Liu, G. Tang and W.-T. Geng, *Comput. Phys. Commun.*, 2021, **267**, 108033.
11. P. Caprioglio, M. Stolterfoht, C. M. Wolff, T. Unold, B. Rech, S. Albrecht and D. Neher, *Adv. Energy Mater.*, 2019, **9**, 201901631.
12. W. Shockley and H. J. Queisser, *J. Appl. Phys.*, 1961, **32**, 510-519.
13. T. Leijtens, R. Prasanna, K. A. Bush, G. E. Eperon, J. A. Raiford, A. Gold-Parker, E. J. Wolf, S. A. Swifter, C. C. Boyd, H.-P. Wang, M. F. Toney, S. F. Bent and M. D. McGehee, *Sustainable Energy Fuels*, 2018, **2**, 2450-2459.
14. R. Lin, J. Xu, M. Wei, Y. Wang, Z. Qin, Z. Liu, J. Wu, K. Xiao, B. Chen, S. M. Park, G. Chen, H. R. Atapattu, K. R. Graham, J. Xu, J. Zhu, L. Li, C. Zhang, E. H. Sargent and H. Tan, *Nature*, 2022, **603**, 73-78.
15. Y. Wang, S. Gu, G. Liu, L. Zhang, Z. Liu, R. Lin, K. Xiao, X. Luo, J. Shi, J. Du, F. Meng, L. Li, Z. Liu and H. Tan, *Sci. China Chem.*, 2021, **64**, 2025-2034.
16. C. Chen, Z. Song, C. Xiao, D. Zhao, N. Shrestha, C. Li, G. Yang, F. Yao, X. Zheng, R. J. Ellingson, C.-S. Jiang, M. Al-Jassim, K. Zhu, G. Fang and Y. Yan, *Nano Energy*, 2019, **61**, 141-147.
17. R. J. Stoddard, A. Rajagopal, R. L. Palmer, I. L. Braly, A. K. Y. Jen and H. W. Hillhouse, *ACS Energy Lett.*, 2018, **3**, 1261-1268.
18. X. Shen, B. M. Gallant, P. Holzhey, J. A. Smith, K. A. Elmestekawy, Z. Yuan, P. V. G. M. Rathnayake, S. Bernardi, A. Dasgupta, E. Kasparavicius, T. Malinauskas, P. Caprioglio, O. Shargaieva, Y. H. Lin, M. M. McCarthy, E. Unger, V. Getautis, A.

Widmer-Cooper, L. M. Herz and H. J. Snaith, *Adv. Mater.*, 2023, **35**, 202211742.

19. Z. Li, J. Zhang, S. Wu, X. Deng, F. Li, D. Liu, C. C. Lee, F. Lin, D. Lei, C.-C. Chueh, Z. Zhu and A. K. Y. Jen, *Nano Energy*, 2020, **78**, 105377.
20. C. Wang, W. Shao, J. Liang, C. Chen, X. Hu, H. Cui, C. Liu, G. Fang and C. Tao, *Small*, 2022, **18**, 202204081.
21. W. Chen, Y. Zhu, J. Xiu, G. Chen, H. Liang, S. Liu, H. Xue, E. Birgersson, J. W. Ho, X. Qin, J. Lin, R. Ma, T. Liu, Y. He, A. M.-C. Ng, X. Guo, Z. He, H. Yan, A. B. Djurišić and Y. Hou, *Nat. Energy*, 2022, **7**, 229-237.
22. Y.-H. Chiang, K. Frohna, H. Salway, A. Abfalterer, L. Pan, B. Roose, M. Anaya and S. D. Stranks, *ACS Energy Lett.*, 2023, **8**, 2728-2737.
23. J. Wen, Y. Zhao, Z. Liu, H. Gao, R. Lin, S. Wan, C. Ji, K. Xiao, Y. Gao, Y. Tian, J. Xie, C. J. Brabec and H. Tan, *Adv. Mater.*, 2022, **34**, 202110356.
24. R. Lin, Y. Wang, Q. Lu, B. Tang, J. Li, H. Gao, Y. Gao, H. Li, C. Ding, J. Wen, P. Wu, C. Liu, S. Zhao, K. Xiao, Z. Liu, C. Ma, Y. Deng, L. Li, F. Fan and H. Tan, *Nature*, 2023, **620**, 994-1000.
25. R. He, Z. Yi, Y. Luo, J. Luo, Q. Wei, H. Lai, H. Huang, B. Zou, G. Cui, W. Wang, C. Xiao, S. Ren, C. Chen, C. Wang, G. Xing, F. Fu and D. Zhao, *Adv. Sci.*, 2022, **9**, 202203210.
26. W. Wang, X. Liu, J. Wang, C. Chen, J. Yu, D. Zhao and W. Tang, *Adv. Energy Mater.*, 2023, **13**, 202300694.
27. H. Lai, J. Luo, Y. Zwirner, S. Olthof, A. Wieczorek, F. Ye, Q. Jeangros, X. Yin, F. Akhundova, T. Ma, R. He, R. K. Kothandaraman, X. Chin, E. Gilshtein, A. Müller, C. Wang, J. Thiesbrummel, S. Siol, J. M. Prieto, T. Unold, M. Stolterfoht, C. Chen, A. N. Tiwari, D. Zhao and F. Fu, *Adv. Energy Mater.*, 2022, **12**, 202202438.
28. S. Li, Z. Zheng, J. Ju, S. Cheng, F. Chen, Z. Xue, L. Ma and Z. Wang, *Adv. Mater.*, 2023, **36**, 202307701.
29. J. Zhu, Y. Luo, R. He, C. Chen, Y. Wang, J. Luo, Z. Yi, J. Thiesbrummel, C. Wang, F. Lang, H. Lai, Y. Xu, J. Wang, Z. Zhang, W. Liang, G. Cui, S. Ren, X. Hao, H. Huang, Y. Wang, F. Yao, Q. Lin, L. Wu, J. Zhang, M. Stolterfoht, F. Fu and D. Zhao, *Nat. Energy*, 2023, **8**, 714-724.
30. Y. Zhao, C. Wang, T. Ma, L. Zhou, Z. Wu, H. Wang, C. Chen, Z. Yu, W. Sun, A. Wang, H. Huang, B. Zou, D. Zhao and X. Li, *Energy Environ. Sci.*, 2023, **16**, 2080-2089.
31. Q. Jiang, J. Tong, R. A. Scheidt, X. Wang, A. E. Louks, Y. Xian, R. Tirawat, A. F. Palmstrom, M. P. Hautzinger, S. P. Harvey, S. Johnston, L. T. Schelhas, B. W. Larson,

E. L. Warren, M. C. Beard, J. J. Berry, Y. Yan and K. Zhu, *Science*, 2022, **378**, 1295-1300.

32. H. Chen, A. Maxwell, C. Li, S. Teale, B. Chen, T. Zhu, E. Ugur, G. Harrison, L. Grater, J. Wang, Z. Wang, L. Zeng, S. M. Park, L. Chen, P. Serles, R. A. Awni, B. Subedi, X. Zheng, C. Xiao, N. J. Podraza, T. Filleter, C. Liu, Y. Yang, J. M. Luther, S. De Wolf, M. G. Kanatzidis, Y. Yan and E. H. Sargent, *Nature*, 2022, **613**, 676-681.
33. Z. Yi, W. Wang, R. He, J. Zhu, W. Jiao, Y. Luo, Y. Xu, Y. Wang, Z. Zeng, K. Wei, J. Zhang, S.-W. Tsang, C. Chen, W. Tang and D. Zhao, *Energy Environ. Sci.*, 2024, **17**, 202-209.
34. F. Yang, P. Tockhorn, A. Musiienko, F. Lang, D. Menzel, R. Macqueen, E. Köhnen, K. Xu, S. Mariotti, D. Mantione, L. Merten, A. Hinderhofer, B. Li, D. R. Wargulski, S. P. Harvey, J. Zhang, F. Scheler, S. Berwig, M. Roß, J. Thiesbrummel, A. Al-Ashouri, K. O. Brinkmann, T. Riedl, F. Schreiber, D. Abou-Ras, H. Snaith, D. Neher, L. Korte, M. Stolterfoht and S. Albrecht, *Adv. Mater.*, 2023, **36**, 202307743.
35. H. Cui, L. Huang, S. Zhou, C. Wang, X. Hu, H. Guan, S. Wang, W. Shao, D. Pu, K. Dong, J. Zhou, P. Jia, W. Wang, C. Tao, W. Ke and G. Fang, *Energy Environ. Sci.*, 2023, **16**, 5992-6002.